Arousal and locomotion differently modulate activity of somatostatin neurons across cortex

Christine F. Khoury[1,2], Noelle G. Fala[2], Caroline A. Runyan*[1,2]

[1]Center for the Neural Basis of Cognition, [2]Department of Neuroscience, University of Pittsburgh

*Corresponding Author: Caroline A. Runyan, runyan@pitt.edu

Number of Pages:

Number of Figures: 6

Number of Tables: 6

Number of words for abstract: 208

Number of words for introduction: 840

Number of words for discussion: 1315

Conflict of Interest Statement: The authors declare no competing financial interests.

Acknowledgments: We thank Chengcheng Huang, Ross Williamson, and members of the Runyan lab for comments on the manuscript. This research was supported in part by the University of Pittsburgh Center for Research Computing through the resources provided. Judith Joyce Balcita-Pedicino performed histology and immunohistochemistry. We thank the GENIE project (Janelia) for making GCaMP sensors available for use. We thank the developers of Suite2P and Wavesurfer. This work was supported by the Andrew W. Mellon Predoctoral Fellowship, NIH Predoctoral Training Grant in Basic Neuroscience (T32 NS007433-21), Pew Biomedical Scholars Program, the Searle Scholars Program, the Klingenstein-Simons Fellowship Award in Neuroscience, and NIH grants NIMH DP2MH122404, NINDS R01NS121913.

Abstract

Arousal powerfully influences cortical activity, in part by modulating local inhibitory circuits. Somatostatin-expressing inhibitory interneurons (SOM) are particularly well-situated to shape local population activity in response to shifts in arousal, yet the relationship between arousal state and SOM activity has not been characterized outside of sensory cortex. To determine whether SOM activity is similarly modulated by behavioral state across different levels of the cortical processing hierarchy, we compared the behavioral modulation of SOM neurons in auditory cortex (AC), a primary sensory region, and posterior parietal cortex (PPC), an association-level region of cortex. Behavioral state modulated activity differently in AC and PPC. In PPC, transitions to high arousal were accompanied by large increases in activity across the full PPC neural population, especially in SOM neurons. In AC, arousal transitions led to more subtle changes in overall activity, as individual SOM and Non-SOM neurons could be either positively or negatively modulated during transitions to high arousal states. The coding of sensory information in population activity was enhanced during periods of high arousal in AC, but not PPC. Our findings suggest unique relationships between activity in local circuits and arousal across cortex, which may be tailored to the roles of specific cortical regions in sensory processing or the control of behavior.

Significance statement: The effects of arousal on brain networks are profound, but vary across regions. Somatostatin neurons may carry out some of the effects of arousal on local network activity in sensory cortex, by modulating response gain and decorrelating population activity. However, SOM neurons have not been well studied outside of sensory cortex, and so it is unknown whether SOM neurons are similarly affected by shifts in brain state throughout the cortex. Here, we have revealed specialization in the relationship between arousal and activity in SOM neurons that could contribute to the diversity of arousal-related impacts on local computation across cortical regions.

Introduction

Arousal profoundly impacts brain activity, at both local and global scales (Livingstone and Hubel, 1981; Marrocco et al., 1994; Cantero et al., 1999; Gould et al., 2011; Grent-'t-Jong et al., 2011; Stringer et al., 2019), and affects sensory perception by tailoring sensory processing to match behavioral demands (Pinto et al., 2013; McGinley et al., 2015; Kuchibhotla et al., 2016; Dadarlat and Stryker, 2017). In sensory cortex, the response gain and signal to noise ratio of individual neurons' responses to sensory stimuli are enhanced with arousal (Niell and Stryker, 2010; Bennett et al., 2013; Polack et al., 2013; Fu et al., 2014; McGinley et al., 2015; Vinck et al., 2015; Mineault et al., 2016). At the population level, activity across neurons becomes decorrelated (Poulet and Petersen, 2008; Zhou et al., 2014; Vinck et al., 2015; Lin et al., 2019), which can enhance the encoding of sensory information by reducing redundancy and correlated noise (Averbeck et al., 2006).

In sensory cortex, these effects can be triggered by the release of neuromodulators linked to arousal, such as norepinephrine and acetylcholine, which act in part through inhibitory interneurons to influence local activity patterns (Fu et al., 2014; Chen et al., 2015; Kuchibhotla et al., 2016; Garcia-Junco-Clemente et al., 2019). The inhibitory cell class can be divided into three nonoverlapping subtypes, which express parvalbumin (PV), somatostatin (SOM), or vasoactive intestinal peptide (VIP), and exhibit distinct local connectivity patterns (Tremblay et al., 2016). SOM neurons are particularly sensitive to arousal state fluctuations, through direct activation of cholinergic and noradrenergic receptors (Kawaguchi and Shindou, 1998; Xiang et al., 1998; Beierlein et al., 2000; Fanselow et al., 2008; Chen et al., 2015; Kuchibhotla et al., 2016), and through inhibition by VIP neurons (Pfeffer et al., 2013; Pi et al., 2013; Fu et al., 2014; Karnani et al., 2016; Dipoppa et al., 2018) . In turn, SOM neurons can powerfully influence local network activity, as they densely innervate the local excitatory population (Fino and Yuste, 2011; Pfeffer et al., 2013; Xu et al., 2013). When they are active, SOM neurons enhance stimulus selectivity and response reliability (Adesnik et al., 2012; Wilson et al., 2012; Rikhye et al., 2021), control local

population activity dynamics (Chen et al., 2015; Veit et al., 2017), and flexibly modulate excitatory responses to stimuli, based on behavioral relevance (Kato et al., 2015; Wang and Yang, 2018).

The impacts of arousal on sensory perception, and on coding in sensory cortex, have been well studied (Fu et al., 2014; Zhou et al., 2014; McGinley et al., 2015; Vinck et al., 2015; Pakan et al., 2016). It is unclear though how specialized or generalized the relationship between arousal and local inhibitory circuit function is across the cortical hierarchy. For example, while arousal- and attention-mediated reductions in shared variability seem to improve sensory coding (Cohen and Maunsell, 2009; Goard and Dan, 2009), similar effects could be detrimental in the read-out of perceptual decisions to control behavior in higher cortex (Runyan et al., 2017; Valente et al., 2021). The basic structure of local circuits is highly conserved across cortical regions, yet differences in neuromodulatory receptor expression, the density of specific cell types, or in the specifics of local connectivity can alter the influence of neuromodulatory input on the pattern of neural population activity. Indeed, the density of SOM neurons is increased relative to PV neurons in association cortex (Kim et al., 2017; Dienel et al., 2020), suggesting that the population-level computations that SOM neurons participate in, and thus the relationship between arousal state and local network state, may differ across the cortical processing hierarchy.

Here, we hypothesized that arousal-related modulation of SOM neurons, and of local neural activity, would be specialized across cortical regions to match different arousal-related demands on local computation. We examined the effects of arousal state on activity in SOM and Non-SOM neurons in the primary auditory cortex (AC), and in the posterior parietal cortex (PPC). AC is a primary sensory region of the cortex, where the relationship between arousal and neural activity has been well studied (Schneider et al., 2014; Zhou et al., 2014; McGinley et al., 2015; Bigelow et al., 2019; Yavorska and Wehr, 2021). PPC is an association-level region that participates in flexible sensorimotor transformations (Fitzgerald et al., 2011; Harvey et al., 2012; Morcos and Harvey, 2016; Licata et al., 2017; Tseng et al., 2022). In PPC, task engagement is known to impact the structure of local population activity (Runyan et al., 2017; Pho et al., 2018; Valente et al., 2021), though relatively little is known about the specific contribution of

generalized increases in arousal to PPC's activity. Outside of a task context, firing rates of neurons in PPC are positively correlated with arousal level (Stitt et al., 2018), but the effects of arousal on specific inhibitory neuron types within PPC are not known. In the current study, we have revealed different relationships between arousal state, the structure of local population activity, and information coding in AC and PPC, suggesting that the effects of arousal on local processing are specialized across the cortical hierarchy.

Materials and Methods

1.0 Experimental Design and Statistical Analysis

All pairwise comparisons were done with two-sided paired or unpaired permutation (i.e. randomization) tests with 10,000 iterations as indicated, where $p<0.0001$ indicates the highest significance achievable given the number of iterations performed. Given that the exact p value is unknown in these cases, p values of the highest significance are reported as such rather than as an exact value. All permutation tests were performed for differences in means. For statistical comparisons involving more than two groups, we used Kruskal-Wallis (non-parametric ANOVA) and used unpaired permutation tests post-hoc to determine which groups differed from each other. Data fell into natural groupings by 1) brain area (AC or PPC) and by 2) cell-type (SOM or Non-SOM), as indicated by expression of the red fluorophore, tdTomato. All bar plots show mean and bootstrapped 95% confidence intervals using 1000 iterations unless otherwise indicated. When multiple comparisons were made between groups, significance thresholds were Bonferroni-corrected. Sample sizes were chosen based on previous studies comparing population activity dynamics across brain areas or cell types (Runyan et al., 2017; Khan et al., 2018).

2.0 Animals

All procedures were approved by the University of Pittsburgh Institutional Animal Care and Use Committee. Homozygous SOM-Cre mice (Sst-IRES-Cre, JAX Stock #013044) were crossed with homozygous Ai14 mice (RCL-tdT-D, JAX Stock #007914) obtained from Jackson Laboratory, ME,

119 USA, and all experiments were performed in the F1 generation, which expressed tdTomato in SOM+
120 neurons. Mice were group housed in cages with between 2 and 4 mice. Adult (8-24 weeks) male and
121 female mice were used for experiments (4 male, 2 female). Mice were housed on a reversed 12 hr
122 light/dark cycle, and all experiments were performed in the dark (active) phase.

123 *2.1 Surgical procedures*

124 Mice were anesthetized with isoflurane (4% for induction, and 1-2% maintenance during surgery), and
125 mounted on a stereotaxic frame (David Kopf Instruments, CA). Ophthalmic ointment was applied to
126 cover the eyes (Henry Schein, NY). Dexamethasone was injected 12-24 hours prior to surgery, and
127 carprofen and dexamethasone (Covetrus, ME) were injected subcutaneously immediately prior to surgery
128 for pain management and to reduce the inflammatory response. Two 2 x 2 mm craniotomies were made
129 over left AC and PPC (centered at 2 mm posterior and 1.75 mm lateral to bregma). For AC, the
130 craniotomy was centered on the temporal ridge, and the posterior edge was aligned with the lamboid
131 suture. 2mm biopsy punches were used to outline the circumference of the window before drilling.

132 1-4 evenly spaced ~60 nl injections of the AAV1-synapsin-l-GCamp6f (Addgene, MA stock #100837)
133 that had been diluted to a titer of ~1x10^12 vg/mL using sterile PBS were made in each cranial window,
134 centered in each craniotomy. A micromanipulator (QUAD, Sutter, CA) was used to target injections ~250
135 µm under the dura at each site, where ~60 nl virus was pressure-injected over 5-10 minutes. Pipettes were
136 not removed until 5 minutes post-injection to prevent backflow. Dental cement (Parkell, NY) sealed a
137 glass coverslip (3mm) over a drop of Kwik Sil (World Precision Instruments, FL) over the craniotomy.
138 Using dental cement, a one-sided titanium headplate was attached to the right hemisphere of the skull.
139 After mice had recovered from the anesthesia, they were returned to their home cages, and received oral
140 carprofen tablets (Bio-Serv, NJ) for 3 days post-surgery.

141 **3.0 Experimental Setup**

142 *3.1 Two-photon microscope*

143 Images were acquired using a resonant scanning two-photon microscope (Ultima Investigator, Bruker,
144 WI) at a 30 Hz frame rate and 512 x 512 pixel resolution through a 16x water immersion lens (Nikon
145 CF175, 16X/0.8 NA, NY). On separate days, either AC or PPC was imaged at a depth between 150 and
146 300 μm, corresponding to layers 2/3 of cortex. For AC imaging, the objective was rotated 35-45 degrees
147 from vertical, and for PPC imaging, it was rotated to 5-15 degrees from vertical, matching the angle of the
148 cranial window implant. Fields of view were 500 μm^2 and contained 187±95 neurons, 20±10 (mean and
149 standard deviation) of which were classified as SOM. Excitation light was provided by a femtosecond
150 infrared laser (Insight X3, Spectra-Physics, CA) tuned to 920 nm. Green and red wavelengths were
151 separated through a 565 nm lowpass filter before passing through bandpass filters (Chroma, ET525/70
152 and ET595/50, VT). PrairieView software (v5.5, Bruker, WI) was used to control the microscope.

153 *3.2 Behavioral monitoring*

154 Running velocity was monitored on pitch and roll axes using two optical sensors (ADNS-98000, Tindie,
155 CA) held adjacent to the spherical treadmill. A microcontroller (Teensy, 3.1, Adafruit, NY)
156 communicated with the sensors, demixing their inputs to produce one output channel per rotational axis
157 using custom code. Outputs controlling the galvanometers were synchronized with running velocity using
158 a digital oscilloscope (Wavesurfer, Janelia, VA).

159 Pupil images were acquired at 1280 x 1024 pixels, at 10 Hz from an infrared (IR) camera focused on one
160 eye (Flea3 FL3-U3-13Y3M-C ½" Monochrome USB 3.0 Camera, 1.0x SilverTL Telecentric Lens, FOV
161 = 6.74mm X 5.39mm, Edmund Optics, NJ). The pupil was illuminated by the IR light emitted by the two-
162 photon laser and required no additional IR illumination. Movies were acquired with the Matlab Image
163 Acquisition Toolbox (Mathworks, MA). Pupil area was determined in each pupil movie frame post-hoc
164 using custom Matlab code (Mathworks, MA). The pupil was constricted by controlling ambient
165 illumination with an array of LCD screens (LG LP097QX1, South Korea), to maintain a moderate pupil
166 area baseline from which increases and decreases in area could be measured.

3.3 Experimental protocol

Imaging began 3-5 weeks post-surgery once robust expression of the GCaMP6f virus was observed. In each imaging session, GCaMP6f fluorescence changes were imaged in SOM (tdTomato+) and Non-SOM neurons, while mice ran freely on a spherical treadmill. In the spontaneous context, no sensory stimuli were delivered, while in the passive listening context, location-varying sound stimuli were presented (see Methods section 3.4). Spontaneous and passive listening contexts lasted ~25-50 minutes each. Imaging alternated between AC and PPC across days. Multiple imaging sessions were performed in each cranial window, focusing at slightly different depths and lateral/posterior locations within the imaging windows across sessions. AC and PPC were each imaged in six mice (biological replicates). Each cranial window was imaged up to 11 times (technical replicates). Imaging from a given cranial window was suspended when we observed nuclear inclusion in 2 or more cells in the field of view, which indicates an over-expression of GCaMP6f.

3.4 Sound stimuli

Four magnetic speakers were positioned in a semicircular array, centered on the mouse's head (MF1-S, Tucker-Davis, FL). The speakers were positioned at -90, -30,+30 and +90 degrees from the midline in azimuth and driven by Matlab through a digital/analog converter (National Instruments). Speakers were calibrated to deliver similar sound levels (~70 db) in a sound isolation chamber using a random incidence microphone (4939, Brüel & Kjær, Denmark). During passive listening, 1 or 2 second dynamic ripples (broadband stimuli created in Matlab by summing 32 tones spaced across 2-32 kHz, which fluctuated at 10-20 Hz (Elhilali et al., 2004) were presented from one of eight locations. Four of the sound locations corresponded to the locations of the four speakers (-90, -30, +30, +90 degrees), while the other four sound locations (-60, -15, +15, +60 degrees) were simulated using vector-based intensity panning, where the same sound stimulus was delivered to two neighboring speakers simultaneously, scaled by a gain factor (Runyan et al., 2017). Dynamic ripples were chosen to optimally drive populations of neurons in auditory

cortex with diverse frequency tuning preferences. Each sound repeated three times at one location before switching to another. Each ripple played from each of the eight locations in randomized order, with a 240 ms gap between each sound. Output controlling the audio speakers recorded along with two-photon imaging galvo and running velocity using Wavesurfer (Janelia, VA), and these signals were aligned offline.

4.0 Data Processing

Imaging datasets from 24 AC fields of view and 20 PPC fields of view were included from 6 mice. We excluded any datasets with significant photobleaching or more than two filled cells. We also excluded any AC or PPC dataset from analysis if fewer than 1/3 of neurons that were significantly responsive (according to our definition in section 5.1) to at least one sound location, as we were interested in the effect of arousal on both spontaneous and sound-evoked responses. For AC datasets, we analyzed single-cell responses to pure tones on a subset of fields of view from each mouse, and then anatomically aligned all fields of view from datasets collected from each window, to ensure each field of view lay in a region representing tone frequencies in the sonic range of the tonotopic axis of primary auditory cortex. We eliminated any datasets where >50% of tone-responsive neurons had a preferred frequency was in the ultrasonic range (>20kHz), as well as any fields of view that were aligned anterior to a field of view where this was observed, to assure that we were seeing sound responses in the range of frequencies primarily represented by our dynamic ripples (described in section 3.4). We collected widefield fluorescence responses to pure tones in all AC cranial windows and observed pure tone responses in the sonic range for all AC windows; however, the extent of the viral expression within windows was too spatially limited to allow for mapping of specific regions.

4.1 Image Processing

For each field of view, the raw calcium movies collected during the spontaneous activity and passive listening contexts were concatenated prior to motion correction, cell body identification, and fluorescence

and neuropil extraction. These processing steps were performed using Suite2p 0.9.3 in Python (Pachitariu et al., 2017). Suite2p first registered images to eliminate brain motion, and clustered neighboring pixels with similar time courses into regions of interest (ROIs). ROIs were manually curated using the Suite2p GUI, to ensure that only cell bodies as opposed to dendritic processes were included in analysis, based on morphology. Cells expressing tdTomato (SOM cells), were identified using a threshold applied in the Suite2p GUI based on mean fluorescence in the red channel after bleed-through correction applied by Suite2p's cell detection algorithm, along with manual correction. For each ROI, Suite2p returned a raw fluorescence timeseries, as well as an estimate of neuropil fluorescence that could contaminate the signal. For each cell, we scaled the neuropil fluorescence by a factor by 0.7 and subtracted this timeseries from the ROI's raw fluorescence timeseries to obtain a neuropil-corrected fluorescence signal for each selected cell.

4.2 ΔF/F and deconvolution

Once the neuropil corrected fluorescence was obtained for each neuron, we calculated ΔF/F for each cell in each frame by calculating $(F-F_{baseline})/F_{baseline}$ for each frame, where F is the fluorescence of a given cell at that frame and $F_{baseline}$ was the eighth percentile of that cell's fluorescence spanning 450 frames before and after (~15s each way, 30 s total). ΔF/F timeseries were then deconvolved to estimate the relative spike rate in each imaging frame using the OASIS toolbox (Friedrich et al., 2017). We used the AR1 FOOPSI algorithm and allowed the toolbox to optimize the convolution kernel, baseline fluorescence, and noise distribution. A threshold of 0.05 a.u. was applied to remove all events with low magnitude from deconvolved activity timeseries. All analyses were performed with both ΔF/F and deconvolved activity, and showed the same trends. Outside of Figure 1F and 1H only results using deconvolved activity are shown.

5.0 Single cell modulation by sound stimuli, running behavior, and pupil size

5.1 Sound responsiveness

Each neuron's deconvolved activity was z-scored across its entire timeseries, and trial-averaged. For each sound location, we then calculated the sound-evoked response as the difference between the mean activity during the sound presentation and the mean activity in the 240 milliseconds prior to sound onset. We then compared the evoked sound responses to shuffled distributions, where each cell's activity was shifted randomly by at least 5 seconds in time relative to sound location time series, and the sound-evoked response was recalculated. This was repeated 1000 times. A neuron was considered to be sound responsive if it had a sound-evoked response at least one sound location that was greater than the 97.5th percentile of the shuffled distribution.

5.2 Running bouts and modulation

Running bout onsets were defined as transitions in speed from below 10 cm/s to above 10 cm/s, and required that the mean running speed in the 1 s following the transition was three times greater than the 1 s prior to running bout onset, and that the mouse maintained a minimum speed of 15 cm/s for the following two seconds.

Running modulation was calculated as the difference in mean activity of a cell in the 1 s prior to running bout onset and the mean activity of a cell in the 3 s window following running bout onset. A shuffling procedure was applied to determine which cells were positively, negatively, and not modulated by running. Each cell's activity was shifted randomly by at least 5 seconds in time relative to running speed timeseries, and for 1000 time-shifted iterations, running modulation was recalculated. Positively modulated neurons had positive running modulation values higher than the 97.5th percentile of that cell's shuffled distribution. Negatively modulated cells had negative running modulation values lower than the 2.5th percentile of that cell's shuffled distribution. All other cells were considered to be not modulated by running speed increases.

5.3 Pupil dilation events and modulation

Pupil area was normalized to its maximum across the imaging session. To identify pupil dilation events, we first identified all local maxima of the pupil area. We then found the point prior to this where the derivative of pupil area was zero. We included events where the time from the inflection point to the local maximum was at least a 40% increase in pupil area and that the change from inflection point to local maximum was less than 1 second, and that the local maximum was at least 50% of the maximum total area by the pupil during that imaging session. We considered each inflection point to be the onset of dilation events.

To capture all pupil dilation related activity, which had a slower time course than running (Figure 4), we calculated pupil modulation for each neurons as the difference between the mean activity in the 1-s time window prior to dilation event onset and the mean activity in the 5-s time window following dilation event onset. We applied the same shuffling procedure as described for running modulation (5.2) to determine which neurons were positively, negatively, and not modulated by pupil dilation events.

6.0 Arousal States

6.1 Defining low and high arousal states based on pupil area

K-means clustering was applied to the full pupil area timeseries, which included both spontaneous activity and passive listening contexts, to classify each pupil area measurement as low, transitional, or high arousal. Each pupil area timeseries was mean normalized using the following equation:

$$\frac{x - \bar{x}}{\bar{x}}$$

The Manhattan (aka City Blocks) distance metric was applied to define 2 centroid clusters that served as the high and low arousal groups. Transition periods included timepoints when the absolute difference in distance to the high and low arousal centroids was less than 0.05.

6.2 Arousal Modulation Index

The arousal modulation index was calculated for each neuron using the following equation:

$$\frac{FR_{hi} - FR_{lo}}{FR_{hi} + FR_{lo}}$$

where FR_{hi} is the mean response of the neuron in the high arousal state and FR_{lo} is the mean response of the neuron in the low arousal state. We first maximum-normalized the deconvolved activity trace of each neuron across the entire time series. To calculate FR_{hi} (or FR_{lo}), we summed the activity from the high (or low) arousal state and divided by the total time spent in the high (or low) arousal state in the spontaneous context. This index could vary continuously between -1 and +1, where negative values indicate higher activity in the low arousal state, and positive numbers indicate higher activity during the high arousal state.

7.0 Encoding Models

We used an encoding model to disentangle the contributions of pupil size and running speed to the activity of neurons in AC and PPC. In the Generalized Linear Model (GLM), the time-dependent effects of all measured external variables on each neuron's activity were estimated (Pillow et al., 2008; Runyan et al., 2017). Three classes of predictors were used in different combinations to quantify their contributions to neuronal activity: running, pupil size, and sound stimulus predictors. We used a Bernoulli-based GLM to weight various combinations of predictors based on these variables to predict each neuron's binarized activity (timeseries of relative spike rates were thresholded at 0.05). The encoding model is fully described in our previous work (Runyan et al., 2017).

7.1 Pupil size and running predictors

Running velocity was measured at a higher time resolution than imaging and was binned to match the sampling rate of two-photon images (30 Hz). We included the velocity along the pitch and roll axes of the treadmill (relative to the mouse's body axis). Running velocity measurements were separated into four channels, (1) forward, (2) reverse, (3) left, (4) right directions based on rotation along these axes. Running

velocity changes could both precede or follow activity of individual neurons, so time series of running velocity were convolved with four evenly spaced Gaussian basis functions (240 ms half-width at half-height) extending 1s both forward and backward in time (8 basis functions total for each running direction: forward, reverse, left, and right). Changes in pupil area were modeled similarly. Because pupil area changes on a slower timescale, the pupil area trace was convolved with 16 evenly spaced Gaussian basis functions 4 s forward and backward in time to allow for either prediction or response to pupil area changes.

7.2 Sound stimulus predictors

Sound stimuli were delivered from specific sound locations in the passive listening context. For sound stimulus onsets at each of the possible sound locations, 12 evenly spaced Gaussian basis functions (170 millisecond half width at half height) extended 2 s forward in time from each sound onset. First, second, and third repeats were represented separately due to potential adaptation-related effects. This resulted in 12 basis functions per repeat per sound location x 3 repeats x 8 locations for 288 sound predictors.

7.3 GLM fitting and cross-validation procedures

All predictors were maximum normalized before the fitting procedure. Beta coefficients for the predictors were fitted to each neuron's activity individually, using the glmnet package in R (Friedman et al., 2010) with elastic-net regularization, which smoothly interpolated between L_1 and L_2 type regularization according to the value of an interpolation parameter α, such that $\alpha=0$ corresponded to L_2 and $\alpha=1$ corresponded to L_1. We selected $\alpha=.25$.

Trials were randomly split into training (70% of trials) and testing (remaining 30% of trials) sets, while balancing the distribution of sound locations. Fitting was performed on the training set, and within each training dataset, cross-validation folds (3x) were also pre-selected so that sound locations were evenly represented. Model performance (see below, 7.4) was assessed on the test set. Each model was thus fitted and tested on entirely separate data to prevent over-fitting from affecting results. This train/test procedure

was repeated ten times, with random subsamples of the data included in train and test segments. Each model's overall performance was assessed as its mean across all 10 iterations.

7.4 GLM model performance

Each model's performance for each cell was defined as the fraction of explained deviance of each model (compared to the null model). In the null model, only a constant (single parameter) was used to fit the neuron's activity and no time-varying predictors were included. First, we calculated the deviance of the null and behavior model variants (see Methods section 7.5). For each model, the fraction of null model deviance explained by the model (d) was then calculated ((null deviance – model deviance)/null deviance). Deviance calculations were performed on a test dataset (30% of the data), which had not been included in the fitting procedure, and this train/test procedure was repeated ten times on randomly subsampled segments of the data.

7.5 Running and pupil contribution

To identify the unique and separable contributions of running and pupil area on SOM and Non-SOM neurons' activity, we fit three separate models: (1) full behavior model, (2) "no pupil" model, (3) "no running" model. In the full behavior model, all running, pupil, and sound predictors were included to fit each neuron's activity. The "no pupil" model did not include the pupil predictors, and the "no running model" did not include the running predictors. Importantly, this analysis captures only the <u>unique</u> ways that pupil size and running can explain neural activity, where one cannot compensate for the other's contribution.

We estimated the contribution of pupil or running to a neuron's activity that could not be compensated for by the other variables, by comparing the model performance (fraction deviance explained, see Methods section 7.4) in the full vs. no pupil or no running models. The "running contribution" was calculated as the difference in fraction deviance explained of the full model and fraction deviance explained of the no-

running model d_{fb}-d_{nr}. The "pupil contribution" was calculated as the difference in fraction deviance explained of the full model and fraction deviance explained of the no-pupil model d_{fb}-d_{np}.

8.0 Decoding

We used a population decoder to compare the sound location information contained in AC and PPC population activity, and its modulation with arousal state. The details of the decoder that we built to estimate the information about sound stimulus location have been previously described (Runyan et al., 2017). Briefly, for each trial we decoded sound stimulus location from single-trial population activity by computing the probability of external variables (sound location Left/Right category) given population activity. We used Bayes' theorem, relying on population response probabilities estimated through the full behavior GLM and its predictors in that trial, to compute the posterior probability of each possible sound location stimulus. The decoder was "cumulative" in time, as for each time point t, it was based on all imaging frames from the initiation of the trial through time t. The decoded stimulus location at each time t was defined as the stimulus location with the maximum posterior probability, based on individual neurons or on a population of simultaneously imaged neurons. The population could include SOM, Non-SOM, or the "best" neurons. Non-SOM neurons were randomly subsampled 10 times, matching the sample size of SOM neurons in each iteration. The "best" neurons were selected as the n individual neurons with the best decoding performance, where n is the number of SOM neurons simultaneously imaged. Decoder performance was calculated as the fraction of correctly classified trials at each time point.

To compare decoder performance in low and high arousal states, trials were classified as "low" or "high" arousal based on normalized pupil area. Only the first sound repetition of each trial was used. Trials were randomly subsampled in the test set to ensure an even distribution of low and high arousal trials, and sound locations. This random subsample was repeated ten times.

9.0 Sound location sensitivity

To assess the location sensitivity of sound-related activity in SOM and Non-SOM neurons in AC and PPC, trial-averaged responses were used to calculate the "location sensitivity index", based on vector averaging in the preferred sound direction:

$$LSI = \sqrt{\left(\sum_{i=1}^{n} R(\Theta_i)cos(2\Theta_i)^{2} + \sum_{i=1}^{n} R(\Theta_i)sin(2\Theta_i)^{2}\right)} / \sum_{i=1}^{n} R_i$$

where R is the average response during the sound location presentation, and Θ is the sound location from -90 to +90 degrees, indexed by i = 1 to n (8 possible locations). LSI can vary continuously from 0 (unselective) to 1 (selectively responding to only one sound location). Datasets that did not have a minimum of 20 trials for each of the eight sound locations were excluded. Importantly, sounds were played from free-field speakers located at different angles relative to the interaural axis. A high LSI could correspond to true sound location selectivity based on interaural level differences, or to a neuron's specific intensity tuning, due to different sound intensities impinging on the two ears.

11.0 Population-level Analyses

11.1 Defining population activity axes related to sound location and arousal

To determine to what degree sound stimuli and arousal were driving population activity independently of each other in AC and PPC, we computed two axes for each imaging session: a sound location axis, and a pupil axis. The sound location axis was defined as the axis in population activity space that connects the mean response on -90° and +90° trials during the passive listening behavioral context, while the pupil axis was defined as the axis that connects the mean population activity during "low arousal" and "high arousal" periods during the spontaneous behavioral context, as defined by our pupil clustering algorithm. These definitions are analogous to how the "attention axis" is computed in primates (Cohen and Maunsell, 2010; Mayo et al., 2015; Cowley et al., 2020). We then measured the angle between the two vectors with a value from 0° to 90°, where 0° indicates linear dependence between the two subspaces and 90° indicates orthogonality.

11.2 Computing Signal and Noise Correlations

We calculated noise correlations as fluctuations around mean sound responses, therefore we only included neurons that had significant sound responses (See: Figure 1K, Materials and Methods). Because it was rare for a mouse's pupil to remain either in the high or low arousal cluster for the entire duration of a trial including all three sound repeats, we focused our analysis instead on the first repeat of a trial. We binned each neuron's z-scored, deconvolved activity into 15-frame (~500 ms) bins following sound onset. For each trial classified as high or low arousal, each cell's mean sound response to all matching sound location presentations (including low, high, and unclassified trials) was subtracted and trials were concatenated. We computed partial Pearson correlations, discounting the effect of running speed (Matlab function 'partialcorr'), on these traces. Because the ratio of low to high trials was variable across imaging sessions, we subsampled 10 times to balance for matching numbers of high and low trials at each sound location. We only considered imaging sessions in which there were at least 50 matched trials in low and high arousal clusters.

12.0 Histology

After all imaging sessions had been acquired, each mouse was transcardially perfused with saline and then 4% paraformaldehyde. The brain was extracted, cryoprotected, embedded, frozen, and sliced. Once slide mounted, we stained brains with DAPI to be able to identify structure. We used anatomical structure to verify the locations of our injections in AC and PPC.

421 **Results**

422 To determine whether the effects of arousal on local activity are conserved across sensory and association
423 cortex, we compared spontaneous and sensory-evoked activity in auditory cortex (AC) and posterior
424 parietal cortex (PPC) in six mice of both sexes, during spontaneous shifts in the animals' arousal state.
425 We used two-photon calcium imaging in superficial cortex to measure the spike-related activity of
426 neurons positive and negative for the red fluorophore tdTomato, which was expressed transgenically in
427 somatostatin-positive (SOM) neurons (Madisen et al., 2009; Taniguchi et al., 2011). We virally expressed
428 the genetically encoded calcium indicator GCaMP6f in all layer 2/3 neurons of AC and PPC in each
429 mouse (Chen et al., 2013).

430 *Neural activity was modulated by sound stimuli and by behavioral correlates of arousal*

431 During each imaging session, we focused the microscope on either AC or PPC, and imaged neural
432 activity in two contexts. During the "spontaneous" context, the mouse ran freely on the spherical
433 treadmill in the absence of sensory stimulation. During "passive listening", sounds were presented from
434 each of eight possible locations (Figure 1 B-C). In both contexts, mice were head-fixed and allowed to
435 run voluntarily on a spherical treadmill. To track the mouse's behavioral state, running velocity and pupil
436 area were recorded throughout imaging sessions (Figure 1 A-H).

437 We first examined how changes in pupil area and running speed corresponded with changes in activity of
438 individual neurons during the spontaneous context. Throughout imaging sessions, mice transitioned
439 between behavioral states that reflect different arousal states: stillness and running, and pupil constriction
440 and dilation (Figure 1 F, H). To quantify the effect of behavioral state transitions on individual neurons'
441 activity, we identified timepoints during the spontaneous context when either running speed or pupil area
442 increased (Materials and Methods 5.2-5.3). The frequency of running bouts and dilation events was
443 similar during PPC and AC imaging sessions ($p=0.59$ and $p=0.65$ respectively, permutation test, here and
444 throughout unless otherwise noted, see Materials and Methods 1.0). Mice initiated running bouts at a rate

445 of 0.915 bouts per minute [0.749, 1.11] (mean and [bootstrapped 95% confidence interval of the mean],
446 here and throughout, unless otherwise indicated), and pupil dilations at 0.981 [0.857, 1.12] dilations per
447 minute. We observed no difference between AC (N=24) and PPC (N=20) imaging sessions when
448 considering pupil area and running speed during passive listening or spontaneous contexts (passive
449 running speed: p=0.20; spontaneous running speed: p=0.52; passive pupil area: p=0.43; spontaneous pupil
450 area: p=0.73). However, pupil area and running speed tended to be higher in general during the passive
451 listening context (pupil: p=0.0020, running: p<0.0001, paired permutation test, N=44 datasets; Figure S1).

452 To determine how behavioral state affected neuronal activity, we next examined the activity of individual
453 neurons during transitions from stationary to running, in the 'spontaneous context', when no sound
454 stimuli were presented. We compared mean activity of each neuron (deconvolved estimated spike rates,
455 here and throughout) in the 3-s time window following running bout onset to the 1-s time window prior to
456 running bout onset (Figure 1 I, See Materials and Methods 5.2). Pupil size modulation was calculated
457 similarly, based on transitions in pupil area from constricted to dilated (Figure 1 D, J; Materials and
458 Methods, 5.3). We compared each neuron's running and pupil modulation to shuffled distributions, where
459 activity and behavioral data were time-shifted by random intervals, and classified each neuron as
460 positively, negatively, or not modulated by behavioral state transition. Larger proportions of the SOM and
461 Non-SOM populations were positively modulated by both pupil dilations and running bout onsets in PPC
462 than in AC (Figure 1 I-J), suggesting that the effects of arousal on spontaneous activity are not uniform
463 across areas. Among the groups considered, the PPC SOM population had the greatest proportion of
464 neurons modulated by running speed and pupil dilation (Figure 1 I-J).

465 In the passive listening context, sound stimuli were presented from each of eight locations, centered on
466 the mouse's head (Figure 1 B-C, See Materials and Methods 3.4). We chose to manipulate sound location
467 because of PPC's role in spatial auditory processing during active behaviors (Nakamura, 1999). To
468 determine whether each neuron was generally sound responsive, we computed the mean difference in
469 activity during sound presentations and the pre-stimulus periods and compared to a shuffled distribution

470 (Materials and Methods 5.1). We defined neurons as sound responsive if they responded to at least one
471 sound location, more than would be expected from a random distribution obtained by shuffling. As
472 expected, a greater proportion of AC SOM and Non-SOM neurons were sound responsive compared to
473 PPC (39% of AC SOM and 40% of AC Non-SOM; 29% of PPC SOM and 28% of PPC Non-SOM
474 neurons, Figure 1 K). The fraction of sound responsive neurons in AC is similar to the sparse sound
475 encoding population described by others in layer 2/3 of AC (Hromádka et al., 2008). Furthermore, sound-
476 evoked responses in AC Non-SOM neurons were lower when mice were running than when they were
477 stationary ($p<0.05$, Figure S2), as has been reported on extensively by others (Schneider et al., 2014;
478 Bigelow et al., 2019; Yavorska and Wehr, 2021). In PPC, sound-evoked responses were not affected by
479 running behavior.

480 *Sound location coding in AC and PPC*

481 To characterize the sound location sensitivity of responses in AC and PPC during the passive listening
482 context, we computed each neuron's sound location sensitivity index (LSI) (Figure 2 A-D, Materials and
483 Methods 9.0). It is important to note that in the free-field sound stimulation configuration, we cannot
484 distinguish true sound location selectivity from differences in sound intensity tuning. In both AC and
485 PPC, Non-SOM neurons were more sensitive to sound location than SOM neurons ($p<0.0001$, Figure 2B-
486 C). PPC neurons overall were less sensitive than AC neurons (Figure 2D), and PPC sound responses were
487 less reliable than AC sound responses ($p<0.001$; Figure 2E). Interestingly, among neurons with sound
488 location preferences, PPC sound responses were biased toward the lateral locations at +90 (contralateral)
489 and -90 (ipsilateral) degrees, while the distribution of sound location preferences in AC neurons was more
490 uniform (Figure 2F-G). Based on these differences in sound location sensitivity and response reliability,
491 we expected population activity to encode sound location more accurately in AC than PPC.

492 To examine sound location coding at the level of neural populations, we constructed population decoders
493 to predict the most likely sound stimulus location (left vs right) using the activity of different subsets of

494 neurons. Each decoder was based on a Bayesian inversion of an encoding model that related each
495 neuron's activity to sound location and timing, running behavior, and pupil size (Figure 3A, Materials and
496 Methods, 8.0; (Runyan et al., 2017)). The posterior probability of each stimulus location was computed
497 cumulatively at each timepoint using population activity from all previous timepoints in the trial. Decoder
498 performance was quantified as the fraction of trials where the stimulus with the maximal posterior
499 probability matched the actual presented stimulus.

500 First, to compare the overall ability of AC and PPC to represent sound location, we used activity of only
501 the "best" cells (i.e., individual neurons whose activity best decoded sound location) regardless of cell
502 type in the population decoder. The number of best cells used for each dataset was chosen to match the
503 number of SOM neurons imaged during that session. The "best cell" decoder's performance was above
504 chance when using activity from both AC and PPC (Figure 3 C-D, Materials and Methods, 8.0).
505 However, as expected based on the sound location sensitivity of individual neurons (Figure 2), AC
506 decoding accuracy was higher than that of PPC ($p<0.0001$). Next, we compared the SOM and Non-SOM
507 population decoders from each dataset. Within both areas, sound location decoding was similar when
508 using the activity of either SOM or Non-SOM populations (AC: $p=0.82$; PPC: $p=0.56$, unpaired
509 permutation tests, Figure 3 C), and both cell type populations from AC outperformed decoding based on
510 PPC populations ($p<0.0001$, unpaired permutation test, Figure 3 C-D). All cell-type specific, subsampled
511 population decoders performed worse than the decoders based on the n-matched population of "best"
512 neurons ($p<0.0001$, paired permutation test; Figure 3 D, See Materials and Methods 8.0). To summarize,
513 sound location was more accurately decoded from AC population activity than PPC, and SOM and
514 random n-matched Non-SOM subpopulations in both areas were similarly informative about sound
515 location. A sparse code for sound location was especially evident in AC, as small numbers of highly
516 tuned "best" neurons more accurately encoded sound location than the random subsamples of the
517 population. See Table 1 for full values and statistics.

518 *SOM neurons' activity was differently modulated during aroused states in AC and PPC*

Next, we more thoroughly characterized the activity of SOM and Non-SOM neurons during arousal state transitions. We focused these analyses on the spontaneous context, to isolate the effects of state transitions from the effects of sound stimulation on activity. We defined behavioral state transitions as the onset times of "running bouts", when the mouse's running speed rapidly increased (Materials and Methods 5.2). We aligned and averaged the pupil area measurements to running bout onsets, observing that pupil area also increased during running bouts, though with a slower time course (Figure 4 A, gray trace, N=44 imaging sessions). We also aligned and averaged the activity of SOM and Non-SOM populations from AC and PPC to running bout onset (Figure 4 A, colored traces, AC, N=24; PPC, N=20 imaging sessions from 6 mice). In both AC and PPC, mean activity of SOM and Non-SOM neurons increased with the onset of running bouts. However, this increase in activity was weak in AC, due to the prevalence of both positively and negatively modulated SOM and Non-SOM neurons in the AC population (Figure 1I, Figure 4 B). In PPC, Non-SOM and SOM neurons more uniformly increased activity at running onset (Figure 1I, Figure 4 B).

Because of the slow time course of changes in pupil area compared to the more rapid transitions in locomotion (Figure 4 C-D), we also characterized single neuron activity during periods of sustained pupil constriction and dilation. We classified pupil measurements as corresponding to low, transitional, or high arousal states (Figure 4 E, Materials and Methods 6.1), and focused analyses on the low and high arousal states. As expected from the relationship between running speed and pupil area, running speed was higher during the pupil-defined high arousal than low arousal states ($p<0.0001$). Mice ran on average 48.24±4.77 cm/s (mean±SEM) during the high arousal state, and 7.71±1.29 cm/s during the low arousal state ($p<0.0001$, N=44 datasets). SOM and Non-SOM activity was elevated overall in high arousal states ($p<0.0001$ for AC Non-SOM, PPC SOM and Non-SOM, $p=0.0029$ for AC SOM neurons, paired permutation test, Figure 4 E-H). To compare arousal modulation of activity in each population of neurons, we next computed an Arousal Modulation Index (AMI, Materials and Methods 6.2), which could vary from -1 to +1, with -1 indicating greater mean activity in the low arousal period, and +1 indicating greater

activity in the high arousal period. The AMI was higher in PPC than AC neurons ($p<0.0001$, See Table 2 for full values and statistics). Interestingly, the AMI differed by cell type in PPC but not AC. In AC, the AMI was similar in SOM and Non-SOM neurons ($p=0.22$), while in PPC, the AMI was higher in SOM than Non-SOM neurons ($p<0.0001$, Figure 4 I).

Finally, to consider the full time-varying relationship between ongoing neuronal activity and behavioral correlates of arousal, we correlated each neuron's activity to pupil area and running speed, across the entire spontaneous behavioral context (Figure 4 J-K). Consistent with the above analyses based on activity aligned on state transitions, SOM and Non-SOM activity in PPC was more strongly correlated with both running and pupil size than in AC ($p<0.0001$). Within AC, SOM and Non-SOM activity was similarly correlated with the two behavioral measures (pupil area, $p=0.063$; running speed, $p=0.146$), while within PPC the activity of SOM neurons was again more strongly correlated with behavior than was the activity of Non-SOM neurons ($p<0.001$ for both running and pupil, Figure 4 J-K, See Table 3).

Taken together, our results so far indicate that in the absence of sound stimulation, SOM and Non-SOM neurons have heterogeneous activity relationships with arousal state in AC, whether defined by running speed or pupil area. In PPC, neuronal activity was positively modulated with heightened arousal, with a stronger modulation of SOM neurons than Non-SOM neurons.

An encoding model revealed different contributions of running speed and pupil size to single cell activity in AC and PPC

Running speed and pupil area are strongly correlated signals but vary on different timescales (Figure 4 C-D) and have separable effects on neuronal activity (Vinck et al., 2015) . Our analyses of ongoing spontaneous activity in AC and PPC also hint at the possibility of separable effects of pupil area and running speed, as AC Non-SOM neurons' activity was more highly correlated with pupil area than with running speed ($p<0.0001$, paired permutation test).

567 To disentangle the relationships between neuronal activity, running velocity, and pupil area, we used an
568 encoding model approach (Pillow et al., 2008; Park et al., 2014; Runyan et al., 2017) . We constructed a
569 Generalized Linear Model (GLM) that used sound stimulus timing and location, pupil area, and running
570 velocity to predict the responses of individual SOM and Non-SOM neurons in AC and PPC, in the
571 passive listening context (Figure 5A). We note that in the above analyses (Figure 1, Figure 4), we
572 considered only the speed at which the mouse was running in any direction, as increased running speed is
573 correlated with heightened arousal (Fu et al., 2014; Zhou et al., 2014; Vinck et al., 2015; Mineault et al.,
574 2016; Shimaoka et al., 2018). Because PPC neurons' activity can be selective for running direction (Nitz,
575 2006; Whitlock et al., 2012; Runyan et al., 2017; Krumin et al., 2018; Minderer et al., 2019) in the GLM
576 we used running velocity rather than speed to obtain more accurate predictions of each neuron's activity
577 (Materials and Methods 7.0, Figure 5).

578 To determine the relative contributions of pupil area and running velocity to neurons' activity, we
579 separately removed these predictors from the model and measured the decrement in the model's
580 prediction performance. For example, we calculated the pupil size contribution to a given neuron's
581 activity as the difference between the prediction performance of the model with and without the pupil size
582 predictors. We considered this decrement in model performance as the contribution of pupil size to the
583 neuron's activity that is not redundant with running speed (Materials and Methods 7.5). If running
584 velocity and pupil area did not make unique contributions to neuronal activity, running predictors would
585 be able to account for the missing pupil area predictors and vice versa, and the performance of the model
586 would not be degraded compared to the full model that includes both pupil area and running velocity
587 predictors. The model comparison revealed single neuron activity that could be explained distinctly by
588 running and by pupil in both AC and PPC (Figure 5 B-G, note neurons along the pupil and running
589 contribution axes in D-G). While a Kruskal Wallis test indicated that the contribution of pupil size
590 differed among the four cell-type/area combinations, post-hoc tests returned $p>.05$ for all pairwise
591 comparisons (See Table 6 for full values and statistics). In contrast, running contributions were overall

592 stronger in PPC neurons than in AC neurons ($p<0.0001$), and within PPC, running contributions were
593 stronger to SOM than Non-SOM activity ($p<0.001$, Figure 5C, F, G). Within AC, running contributions
594 did not depend on cell type ($p=0.44$, Figure 5C, D, E). See Table 6 for full values and statistics. Thus,
595 running contributions, but not pupil contributions, reflect the observed differences in the arousal-
596 dependence of activity in AC and PPC.

597 *Sound location coding was enhanced with arousal in AC, but not PPC*

598 Given the activity changes with arousal in AC and PPC, we hypothesized that arousal would affect
599 sensory information coding in both regions. To test this possibility, we trained and tested the sound
600 location decoder (Figure 3) in low and high arousal periods (Figure 6 A - E). Sound stimulus trials were
601 classified as occurring during low or high arousal states based on pupil size (as in Figure 4 E), and low
602 and high arousal trials were evenly balanced to train and test the decoders. Decoding performance for left
603 vs. right sound locations using AC populations was modestly improved during heightened arousal
604 ($p=0.0003$, paired permutation test), but decoding performance was similarly poor in low and high arousal
605 trials using PPC population activity (Figure 6 C-E) ($p=0.06$, paired permutation test). Thus, while sensory
606 coding in AC was slightly improved with heightened arousal, coding within PPC populations was
607 unaffected by arousal state. See Table 1 for full values and statistics.

608 To better understand the basis for the improvement in sound location coding with arousal in AC, we
609 related the sound coding of individual neurons (z-scored decoding performance) to the contribution of
610 pupil size to their activity (from the encoding model in Figure 5). In AC, sound coding had a weakly
611 negative relationship with pupil modulation (Pearson's correlation = -0.03), where the neurons with the
612 strongest sound coding tended to have the weakest pupil modulation. In PPC, on the other hand, sound
613 coding and pupil modulation were positively correlated (Pearson's correlation = 0.17), as the same
614 neurons can be modulated by both sound and arousal state in PPC. We then examined the modulation of
615 neural population activity by sounds and by arousal state, in population activity space, where each

616 dimension (axis) is the activity of one neuron and a population of n neurons has n dimensions (axes)
617 (Cunningham and Yu, 2014). We found the direction of the 'sound location axis', along which left vs
618 right sound locations were best distinguished in this n-dimensional space, and the direction of the 'pupil
619 axis', along which pupil size best explained population activity, in each AC and PPC population (See
620 Materials and Methods, 11.1). We then measured the angle between these axes. In AC, these angles were
621 more orthogonal to each other than in PPC ($p=0.0006$).

622 The correlation structure of population activity influences the amount of information that can be encoded
623 across neurons (Averbeck et al., 2006; Panzeri et al., 2022). Specifically, the slope of the relationship
624 between signal and noise correlations determines whether noise correlations limit the information that can
625 be encoded by the population. In other words, greater shared variability among neurons with similar
626 tuning preferences reduces the information that the population can encode. As a consequence, reductions
627 in noise correlations among neuron pairs with similar tuning preferences or increases in noise correlations
628 among neuron pairs with opposing tuning preferences would both theoretically increase the encoding
629 capacity of a neural population (Averbeck et al., 2006; Panzeri et al., 2022). We then wondered whether
630 transitions between arousal states also induced different changes in the correlation structure in AC and
631 PPC, contributing to the improvements in sound location coding in AC. We compared pairwise noise
632 correlations in high and low arousal conditions for both regions, and sorted these by the signal
633 correlations between neuron pairs. Pairwise noise correlations among neurons with similar sound location
634 preferences (high signal correlations) were reduced in the high arousal state in AC ($p=0.002$). In PPC, on
635 the other hand, these similarly tuned neurons instead became more correlated with arousal ($p<0.0001$). In
636 neuron pairs with negative signal correlations (different tuning), noise correlations were enhanced in AC
637 ($p = 0.0015$), but did not change with arousal in PPC ($p = 0.235$). Taken together, the arousal-induced
638 changes in the correlation structure of population activity suggest that the improvement in sound location
639 coding in AC could result from a reduction in shared variability across neurons with similar sound
640 preferences, in addition to the generalized suppression in sound-evoked responses during locomotion

641 (Schneider et al., 2014; Bigelow et al., 2019; Yavorska and Wehr, 2021) that could sharpen response

642 selectivity.

643

Discussion

Our goal in this study was to determine whether the activity of inhibitory interneurons is differently modulated by behavioral state across the cortical processing hierarchy. We have measured spontaneous and sound-driven activity in populations of somatostatin-expressing inhibitory interneurons (SOM) and Non-SOM neurons in layer 2/3 of auditory cortex (AC) and in posterior parietal cortex (PPC), while mice transitioned between arousal states.

In the absence of sound stimulation, the effects of arousal state on spontaneous activity in AC were complex. Although heightened arousal had a slight positive effect on activity in AC at the population level, activity in individual AC neurons could be positively or negatively modulated, as has been described previously by others (Bigelow et al., 2019; Yavorska and Wehr, 2021). Short spurts of running, as we observed in our imaging sessions (Figure S1D), are associated with a net depolarization in AC (Shimaoka et al, 2018), which likely contributes to the net positive relationship between spontaneous AC activity and running observed here. In contrast, the spontaneous activity of most PPC neurons increased during these heightened arousal states, and SOM neurons were even more strongly and uniformly modulated than Non-SOM neurons.

The behavioral state transitions in our study involved increases both in pupil size and in locomotion (Figure 4A). It is thus crucial to emphasize that the effects of heightened arousal state on neural activity described here include a mixture of motor-related and 'true' arousal-related effects, such as those resulting from increases in norepinephrine and acetylcholine release within AC and PPC. While locomotion, whisking, and pupil dilations have all been considered as behavioral correlates of an animal's arousal state, motor-related feedback acts on specialized circuits within visual, somatosensory, and auditory cortices, determining whether motor behavior positively or negatively influences neural activity (Lee et al., 2013; Fu et al., 2014; Schneider et al., 2014; Pakan et al., 2016; Bigelow et al., 2019; Yavorska and Wehr, 2021). This motor-related feedback acts in concert with neuromodulatory inputs

668 more directly related to the animal's arousal state, leading to state-dependent network changes that are
669 specialized across cortical regions. It is unlikely that any aroused state is without a related change in
670 fidgeting, facial movements, or other motor outputs (Musall et al., 2019; Stringer et al., 2019), and so the
671 relative contributions of motor-related vs neuromodulatory inputs to neural activity must be defined for
672 each brain region for a full consideration of state-dependent processing across the cortex. Here, we were
673 able to disentangle the *unique* contributions of running velocity and pupil size to the activity of individual
674 neurons in AC and PPC using an encoding model (Figure 5). In both regions, pupil size and running
675 velocity had distinguishable contributions to the activity of SOM and Non-SOM neurons. The magnitude
676 of unique pupil contributions was similar across all groups, but running contributions to activity were
677 significantly stronger in PPC, particularly among SOM neurons.

678 In AC, the effects of arousal and locomotion can oppose each other, as motor-related feedback activates
679 PV neurons, reducing sound-evoked responses during locomotion (Schneider et al., 2014; Bigelow et al.,
680 2019; Yavorska and Wehr, 2021). We observed a small number of Non-SOM neurons in AC that were
681 strongly and positively modulated with locomotion, which may include the PV neurons mediating the
682 locomotion-related reduction of activity in other neurons (Schneider et al., 2014). In PPC, motor-related
683 effects were largely positive, and were particularly strong among SOM neurons, suggesting that, unlike in
684 AC (Schneider et al., 2014), motor feedback does not target PV neurons in PPC. Instead, SOM neurons in
685 PPC may inhibit PV neurons during locomotion, disinhibiting excitatory neurons and further enhancing
686 the arousal-related increase in activity in the local population. It will be interesting to determine whether
687 this is the case in future studies. Recently, we also discovered that activity within the SOM population is
688 highly coordinated, especially in PPC (Khoury et al., 2022). As a result, the transitions from low to high
689 arousal states would trigger highly coordinated SOM population events, which could strongly impact the
690 local network activity state (Chen et al., 2015; Veit et al., 2017; Wang and Yang, 2018). In the future,
691 causal manipulations of SOM neurons, mimicking their activity during arousal transitions, will help

692 reveal the impact of these coordinated SOM activity events on the activity and coding in the local
693 population.

694 The effects of arousal on stimulus coding have been examined in depth across primary sensory cortices
695 (Zhou et al., 2014; McGinley et al., 2015; Vinck et al., 2015; Shimaoka et al., 2018; Lin et al., 2019).
696 Previous studies revealed that moderate levels of arousal optimally impact sensory coding (McGinley et
697 al., 2015; Lin et al., 2019), aligning well with the Yerkes-Dodson (inverted-U) relationship between
698 arousal and perceptual task performance (Waschke et al., 2019). Unlike these studies, we did not observe
699 a decrement in sound location coding in the highest arousal state, instead measuring a modest
700 improvement in decoding accuracy in the high arousal state. Mice in our experiments were most likely to
701 visit two separable behavioral states (stationary/unaroused or running/aroused), without the gradation of
702 different levels of arousal observed by others. As a result, the "high" arousal state described here likely
703 includes a mixture of the moderate and high arousal states defined by others (McGinley et al., 2015).
704 Because sensory coding in PPC depends on the behavioral relevance of stimuli (Fitzgerald et al., 2011;
705 Pho et al., 2018), we expected that sound coding would also improve in PPC with heightened arousal,
706 when mice might be more aware of the sound stimuli. Surprisingly, despite the more pronounced positive
707 modulation of activity in PPC that accompanied increases in arousal and locomotion (Figure 4), the
708 behavioral state did not affect sensory encoding in PPC (Figure 6). Our results imply that arousal alone is
709 not sufficient to improve sensory coding in PPC outside of a task context, supporting the idea that task
710 engagement and arousal modulate sensory responses through separate pathways (Saderi et al., 2021).

711 Finally, to better understand the basis of the improvement of sound coding with arousal in AC (and lack
712 thereof in PPC), we related sound coding and pupil-related effects on population activity and its
713 correlation structure. In AC, sound coding and pupil modulation were strongest in distinct sets of neurons
714 (Figure 6F), and with heightened arousal, shared variability was reduced among neurons with similar
715 tuning (Figure 6J). The net result was an improvement in our ability to decode sound information from
716 AC population activity in the heightened arousal state, as the responses of the population to different

717 stimuli were more separable (schematized in Figure 6L). In PPC, on the other hand, sound coding and
718 pupil modulation were inter-mixed within the same neurons (Figure 6G), and shared variability *increased*
719 among neurons with similar tuning (Figure 6K). As a consequence, although activity was strongly
720 modulated in PPC with arousal, the separability of population responses to different sounds was not
721 affected (Figure 6M). As has been recently reviewed, positive noise correlations among neurons with
722 similar tuning limit the information that a population can encode (Averbeck et al., 2006; Panzeri et al.,
723 2022), which is consistent with our results. To summarize, arousal had different effects on the correlation
724 structure of population activity in AC and PPC. In AC, the result was better separability of the population
725 responses to different sounds, while in PPC the effects of arousal on population activity were
726 information-limiting (Averbeck et al., 2006; Panzeri et al., 2022).

727 To conclude, we have characterized the effects of the global arousal state on population activity in
728 sensory and association cortex, by measuring neuronal activity during fluctuations in arousal and
729 locomotion. In AC, but not PPC, sensory representations were enhanced with arousal, even when not
730 behaviorally relevant. An important future direction will be to determine whether global shifts in arousal
731 affect the coding of behaviorally relevant information in PPC, and whether local inhibitory circuits can
732 provide a gating mechanism to enhance PPC's encoding of behaviorally relevant sensory information.

733

734 **Figure Legends**

735 **Figure 1: Imaging spike-related activity in SOM and Non-SOM neurons during behavioral state**
736 **transitions**.

737 (A) Viral injections and cranial windows were made over auditory cortex (AC) and posterior parietal
738 cortex (PPC) in each SOM-tdTomato mouse. (B) In imaging sessions, mice were headfixed over a
739 spherical treadmill and allowed to run voluntarily. Four speakers arranged around the head presented
740 sound stimuli. An infrared camera was used to image the pupil, and a rotating two-photon microscope

was focused on either AC or PPC on a given imaging day. (C) Each imaging session included "Spontaneous" and "Passive Listening" contexts, without or with randomly presented sound stimuli from each of eight locations, respectively. (D) Pupil area was monitored via the pupil camera, scalebar in bottom image applies to top (constricted pupil) and bottom (dilated pupil). (E) Example field of view from auditory cortex, with intermingled tdTomato+/SOM+ (magenta) and tdTomato-/SOM- neurons, co-expressing GCaMP6f (green). (F) Example aligned behavioral and neural signals collected during the imaging session in E, including running speed (cm/s), normalized pupil area, dF/F from a Non-SOM (red) and SOM neuron (orange), each overlaid with the neuron's deconvolved estimated spike rates. (G) As in E, for an example posterior parietal cortex field of view. (H) As in F, for the PPC field of view in G. (I) Proportions of Non-SOM and SOM neurons in AC (left) and PPC (right) with significant positive (white), negative (black), or no modulation (gray) by mouse's running onset. AC Non-SOM N=2645; AC SOM N=359; PPC Non-SOM N=4719; PPC SOM N=525. (J) As in I, for pupil dilation. (K) Proportion of Non-SOM and SOM neurons in AC and PPC that were significantly sound responsive to at least one location (white) or not significantly sound responsive (gray).

Figure 2: Sound Location Sensitivity in AC and PPC. (A) Six example neurons with diverse sound location preferences, ranging from ipsilateral (-90 - 0 degrees) to contralateral locations (0 - +90 degrees). Thin lines: mean response during sound presentation of individual trials. Thick lines: Trial average. The Location Sensitivity Index (LSI) and response reliability are reported for each example cell. Red: Example Non-SOM neurons. Orange: Example SOM neuron. (B) Distribution of Location Sensitivity Index (LSI) for Non-SOM (0.20 [0.20, 0.21] , N=2455) and SOM (.19 [0.18, .19], N=354) neurons in AC. Triangles indicate population means. (C) As in B, for PPC Non-SOM (0.20 [0.19, 0.20], N=2553) and SOM (.13 [.12, .14], N=298). (D) Mean Location Sensitivity Index in AC and PPC. (E) Cumulative distributions of response reliability, the fraction of sound-responsive trials, in AC and PPC. (F) Histograms of the preferred locations of all AC Non-SOM and SOM neurons with LSI's>0.05. (G)

765 Histograms of the preferred locations of all PPC Non-SOM and SOM neurons with LSI's>0.05. * p<0.05,
766 ***p<0.001, ****p<0.0001, error bars indicate SEM.

767 **Figure 3: Decoding Sound Location from AC and PPC Population Activity.** (A) The encoding model
768 was trained on all trials that included all arousal levels, and inverted using Bayes Rule to compute the
769 posterior probability of auditory stimuli given the activity of the neural population in AC and PPC . (B)
770 Schematic of the discrimination being performed by the decoder, classifying sound stimuli as occuring
771 from the left or right of the mouse. (C) Left: Mean cumulative population decoder performance (across
772 datasets) when classifying left vs right locations, when based on "best cells", defined as individual Non-
773 SOM cells or SOM cells with the highest decoding performance. "Best cells" and Non-SOM cells in each
774 dataset were subsampled to match the N of the SOM neuron population within each imaging field of
775 view. Right: Population decoder performance using PPC neurons. Chance performance is 0.5. (D) Mean
776 decoder performance using all timepoints in the trial (equivalent to the final timepoints in (C) using SOM
777 neurons, subsampled Non-SOM neurons, and "best cells" in AC and PPC. Dotted line corresponds to
778 chance performance (50%). N=24 AC datasets, N=20 PPC datasets. Error bars indicate SEM.
779 ****p<0.0001.

780 **Figure 4: Single cell activity changes with arousal during the spontaneous context.** (A) Average z-
781 scored deconvolved activity, running speed, and pupil area aligned on running bout onset. Red: AC Non-
782 SOM neurons' activity (N=24 datasets), Orange: AC SOM neurons' activity (N=24 datasets), Dark Blue:
783 PPC Non-SOM neurons' activity (N=20 datasets), Light Blue: PPC SOM neurons' activity (N=20
784 datasets), Black: Running speed (N=44 datasets), Gray: Pupil area (N=44 datasets). (B) Average z-scored
785 deconvolved activity of individual neurons, from L to R: all AC Non-SOM, AC SOM, PPC Non-SOM,
786 and PPC SOM neurons aligned on running bout onset (AC Non-SOM N=2645; AC SOM N=359; PPC
787 Non-SOM N=4719; PPC SOM N=525, in B-I). Neurons were sorted by running modulation. (C)
788 Autocorrelation of pupil area and running speed, averaged across all datasets (N=44). (D) Cross-
789 correlation between running speed and pupil area, averaged across all datasets (N=44). Black triangle

790 indicates time lag with peak correlation, with running preceding pupil by 1.27 s. (E) Illustration of
791 clustering that sorted pupil area during each imaging frame into low, transition, and high arousal states.
792 (F) Mean responses of AC Non-SOM (red solid), AC SOM (red dotted), PPC Non-SOM (blue solid), and
793 PPC SOM (blue dotted) neurons in low and high arousal states, as defined in E. (G) Left: Mean activity of
794 AC Non-SOM neurons in high arousal state (classified with clustering as in E), plotted against mean
795 activity in the low arousal state. Right: Mean activity of AC SOM neurons in high arousal vs low arousal
796 states. (H) As in G, for PPC Non-SOM and SOM neurons. (I) Cumulative probability distribution of the
797 arousal modulation index in AC Non-SOM (solid red), AC SOM (dotted red), PPC Non-SOM (solid
798 blue), and PPC SOM (dotted blue) neurons. Arousal modulation index was calculated from the values in
799 G-H, (High-Low)/(High+Low) for each neuron. (J) Cumulative probability distribution of the Pearson
800 correlation between each neuron's activity and pupil area, colors as in I. (K) Cumulative probability
801 distribution of the Pearson correlation between each neuron's activity and running speed. Significance as
802 indicated, permutation test, **** p<.0001. Error bars: 95% bootstrapped confidence interval around the
803 mean.

804 **Figure 5: Using an Encoding Model to Disentange Running and Pupil Contributions to Single Cell**
805 **Activity.** (A) Schematic of Generalized Linear Model (GLM) used to determine the unique contributions
806 of pupil area and running velocity to neurons' activity. (B) Average contribution of pupil area to activity
807 across all AC Non-SOM (N=2645) and SOM (N=359) neurons (red bars) and PPC Non-SOM (N=4525)
808 and SOM (N=505) neurons (blue bars). Contribution was quantified as the improvement in model
809 prediction performance of each neuron's activity when adding pupil area as a set of predictors. Errorbars
810 indicate SEM, n.s., not significant, exact values in text. (C) As in B, calculated when comparing model
811 performance with and without running velocity predictors. AC Non-SOM and SOM neurons (red bars)
812 and PPC Non-SOM and SOM neurons (blue bars), ****p<.0001. (D) Pupil contribution plotted against
813 running contribution for each AC Non-SOM neuron, calculated as in B. (E) Pupil contribution plotted

814 against running contribution for each AC SOM neuron. (F-G) Pupil contribution plotted against running
815 contribution for each PPC Non-SOM or SOM neuron. Sample sizes in B apply to all panels.

816 **Figure 6: Arousal impacts the structure of population activity, improving information coding in**
817 **AC.** (A) The encoding model was trained on all trials that included all arousal levels, and inverted using
818 Bayes Rule to compute the posterior probability of auditory stimuli given the activity of the neural
819 population in AC and PPC. (B) Schematic of the discrimination being performed by the decoder,
820 classifying sound stimuli as occuring from the left or right of the mouse. (C) Mean fraction correct of
821 cumulative sound location (left sound locations vs right sound locations) decoding in AC (right) and PPC
822 (left) populations in high (dark) and low (light) arousal conditions. Subsampling to match arousal and
823 sound locations was repeated 10x. (D) Cumulative fraction correct of decoding for left vs right sound
824 location at the end of the trial in AC and PPC. (F) For each AC neuron, the sound location decoding
825 performance based on that neuron's activity is plotted against that neuron's pupil modulation, as
826 quantified by the encoding model in Figure 5. Neurons are color-coded from black to red to indicate their
827 z-scored sound location decoding performance (red neurons > 0 z-scored performance). (G) As in F, for
828 PPC. (H) Schematic to explain the definitions of the sound location and pupil axes in high dimensional
829 population activity space in I. (I) Angle in degrees between the pupil and sound location axes in each AC
830 and PPC dataset. The angle between the pupil and sound axes is significantly smaller in PPC than AC. (J)
831 Mean pairwise noise correlation among sound responsive AC neurons during high arousal (gray) and low
832 arousal (black) trials, binned by their pairwise signal correlation. (K) As in (J), but for PPC. (L)
833 Schematic demonstrating the impacts of arousal on sound coding in AC population activity. The shape of
834 the population activity subspace responding to "sound 1" and "sound 2" changes between low arousal
835 (dashed outlines) and high arousal (gray ovals) states, improving their discriminability. This shape change
836 occurs because the shared variability is reduced among neurons coding for similar locations, and
837 enhanced among neurons coding for different locations (see J). (M) As in L, for PPC. In PPC, the shape
838 of the area of population activity space encoding sound 1 or sound 2 does not change with arousal, as

shared variability is more generally increased across neuron pairs (see K). Across panels, ** p<0.01, *** p<0.001, **** p<0.0001, n.s. not significant. AC Non-SOM N=24 datasets; AC SOM N=24 datasets; PPC Non-SOM N=20 datasets; PPC SOM N=20 datasets throughout figure panels.

Supplementary Figures

Figure S1: Characterizing running behavior and pupil size across contexts. (A) Left: Mean running speed in the spontaneous and passive listening behavioral contexts. Right: Mean running speed during the passive listening context plotted against the mean running speed during the spontaneous context, for each imaging session, p=.0003. (B) Left: Mean, maximum normalized pupil area during the spontaneous and passive listening contexts. Right: Mean pupil area in the two contexts for each imaging session. p=.002. (C) Left: Mean time spent running less than 15 cm/s in spontaneous and passive listening contexts. Right: Time spent running less than 15 cm/s during the two contexts, for each imaging session, p<.0001. (D) Left: Mean time spent running faster than15 cm/s in spontaneous and passive listening contexts. Right: Time spent running faster than 15 cm/s in the two contexts, for each imaging session. N=44 imaging sessions for all panels. Error bars indicate bootstrapped 95% confidence intervals, ***p<0.001; **p<.01.

Table Titles/Legends

Table 1: Sound Location Decoding/Full values and statistics related to Figures 3 & 6

Table 2: Arousal Modulation Index during spontaneous context/Full values and statistics related to Figure 4I

Table 3: Correlation coefficients with pupil area and running speed during spontaneous context/Full values and statistics related to Figure 4J-K

Table 4: Arousal Modulation Index during passive listening context

Table 5: Correlation coefficients with pupil area and running speed during passive listening context

Table 6: Pupil and Running Contributions/Full values and statistics related to Figure 5

References

Adesnik H, Bruns W, Taniguchi H, Huang ZJ, Scanziani M (2012) A neural circuit for spatial summation in visual cortex. Nature 490:226–231.

Averbeck BB, Latham PE, Pouget A (2006) Neural correlations, population coding and computation. Nature Reviews Neuroscience 7:358–366.

Beierlein M, Gibson JR, Connors BW (2000) A network of electrically coupled interneurons drives synchronized inhibition in neocortex. Nat Neurosci 3:904–910.

Bennett C, Arroyo S, Hestrin S (2013) Subthreshold Mechanisms Underlying State-Dependent Modulation of Visual Responses. Neuron 80:350–357.

Bigelow J, Morrill RJ, Dekloe J, Hasenstaub AR (2019) Movement and VIP Interneuron Activation Differentially Modulate Encoding in Mouse Auditory Cortex. Eneuro 6:ENEURO.0164-19.2019.

Cantero JL, Atienza M, Salas RM, Gómez CM (1999) Brain Spatial Microstates of Human Spontaneous Alpha Activity in Relaxed Wakefulness, Drowsiness Period, and REM Sleep. Brain Topogr 11:257–263.

Chen N, Sugihara H, Sur M (2015) An acetylcholine-activated microcircuit drives temporal dynamics of cortical activity. Nature Neuroscience 18:892–902.

Chen T-W, Wardill TJ, Sun Y, Pulver SR, Renninger SL, Baohan A, Schreiter ER, Kerr RA, Orger MB, Jayaraman V, Looger LL, Svoboda K, Kim DS (2013) Ultrasensitive fluorescent proteins for imaging neuronal activity. Nature 499:295–300.

Cohen MR, Maunsell JHR (2009) Attention improves performance primarily by reducing interneuronal correlations. Nature Neuroscience 12:1594–1600.

Cohen MR, Maunsell JHR (2010) A Neuronal Population Measure of Attention Predicts Behavioral Performance on Individual Trials. The Journal of neuroscience : the official journal of the Society for Neuroscience 30:15241–15253.

Cowley BR, Snyder AC, Acar K, Williamson RC, Yu BM, Smith MA (2020) Slow Drift of Neural Activity as a Signature of Impulsivity in Macaque Visual and Prefrontal Cortex. Neuron 108:551-567.e8.

Cunningham JP, Yu BM (2014) Dimensionality reduction for large-scale neural recordings. Nat Neurosci 17:1500–1509.

Dadarlat MC, Stryker MP (2017) Locomotion Enhances Neural Encoding of Visual Stimuli in Mouse V1. J Neurosci 37:3764–3775.

Dienel SJ, Ciesielski AJ, Bazmi HH, Profozich EA, Fish KN, Lewis DA (2020) Distinct Laminar and Cellular Patterns of GABA Neuron Transcript Expression in Monkey Prefrontal and Visual Cortices. Cereb Cortex 31:bhaa341-.

Dipoppa M, Ranson A, Krumin M, Pachitariu M, Carandini M, Harris KD (2018) Vision and Locomotion Shape the Interactions between Neuron Types in Mouse Visual Cortex. Neuron 98:602-615.e8.

Elhilali M, Fritz JB, Klein DJ, Simon JZ, Shamma SA (2004) Dynamics of precise spike timing in primary auditory cortex. The Journal of neuroscience : the official journal of the Society for Neuroscience 24:1159–1172.

Fanselow EE, Richardson KA, Connors BW (2008) Selective, state-dependent activation of somatostatin-expressing inhibitory interneurons in mouse neocortex. Journal of neurophysiology 100:2640–2652 Available at: http://jn.physiology.org/cgi/content/full/100/5/2640.

Fino E, Yuste R (2011) Dense Inhibitory Connectivity in Neocortex. Neuron 69:1188–1203 Available at: http://dx.doi.org/10.1016/j.neuron.2011.02.025.

Fitzgerald JK, Freedman DJ, Assad JA (2011) Generalized associative representations in parietal cortex. Nature Neuroscience 14:1075–1079.

Friedman J, Hastie T, Tibshirani R (2010) Regularization Paths for Generalized Linear Models via Coordinate Descent. Journal of Statistical Software 33 Available at: https://www.jstatsoft.org/article/view/v033i01.

Friedrich J, Zhou P, Paninski L (2017) Fast online deconvolution of calcium imaging data. Plos Comput Biol 13:e1005423.

Fu Y, Tucciarone JM, Espinosa JS, Sheng N, Darcy DP, Nicoll RA, Huang ZJ, Stryker MP (2014) A Cortical Circuit for Gain Control by Behavioral State. Cell 156:1139–1152 Available at: https://www.sciencedirect.com/science/article/pii/S0092867414001445.

Garcia-Junco-Clemente P, Tring E, Ringach DL, Trachtenberg JT (2019) State-Dependent Subnetworks of Parvalbumin-Expressing Interneurons in Neocortex. Cell Reports 26:2282-2288.e3.

Goard M, Dan Y (2009) Basal forebrain activation enhances cortical coding of natural scenes. Nature Neuroscience 12:1444–1449 Available at: http://www.nature.com/neuro/journal/v12/n11/abs/nn.2402.html.

Gould IC, Rushworth MF, Nobre AC (2011) Indexing the graded allocation of visuospatial attention using anticipatory alpha oscillations. J Neurophysiol 105:1318–1326.

Grent-'t-Jong T, Boehler CN, Kenemans JL, Woldorff MG (2011) Differential functional roles of slow-wave and oscillatory-α activity in visual sensory cortex during anticipatory visual-spatial attention. Cereb Cortex New York N Y 1991 21:2204–2216.

Harvey CD, Coen P, Tank DW (2012) Choice-specific sequences in parietal cortex during a virtual-navigation decision task. Nature 484:62–68 Available at: http://www.nature.com/nature/journal/v484/n7392/abs/nature10918.html.

Hromádka T, Deweese MR, Zador AM (2008) Sparse representation of sounds in the unanesthetized auditory cortex. PLoS Biology 6:e16 Available at:

935 http://eutils.ncbi.nlm.nih.gov/entrez/eutils/elink.fcgi?dbfrom=pubmed&;id=18232737&retmode=ref&
936 cmd=prlinks.

937 Karnani MM, Jackson J, Ayzenshtat I, Sichani AH, Manoocheri K, Kim S, Yuste R (2016) Opening
938 Holes in the Blanket of Inhibition: Localized Lateral Disinhibition by VIP Interneurons. J Neurosci
939 36:3471–3480.

940 Kato HK, Gillet SN, Isaacson JS (2015) Flexible Sensory Representations in Auditory Cortex Driven by
941 Behavioral Relevance. Neuron 88:1027–1039.

942 Kawaguchi Y, Shindou T (1998) Noradrenergic Excitation and Inhibition of GABAergic Cell Types in
943 Rat Frontal Cortex. J Neurosci 18:6963–6976.

944 Khoury CF, Fala NG, Runyan CA (2022) The spatial scale of somatostatin subnetworks increases from
945 sensory to association cortex. Cell Reports 40:111319.

946 Kim Y, Yang GR, Pradhan K, Venkataraju KU, Bota M, Molino LCG del, Fitzgerald G, Ram K, He M,
947 Levine JM, Mitra P, Huang ZJ, Wang X-J, Osten P (2017) Brain-wide Maps Reveal Stereotyped Cell-
948 Type-Based Cortical Architecture and Subcortical Sexual Dimorphism. Cell 171:456-469.e22.

949 Krumin M, Lee JJ, Harris KD, Carandini M (2018) Decision and navigation in mouse parietal cortex.
950 Elife 7:e42583.

951 Kuchibhotla KV, Gill JV, Lindsay GW, Papadoyannis ES, Field RE, Sten TAH, Miller KD, Froemke RC
952 (2016) Parallel processing by cortical inhibition enables context-dependent behavior. Nature
953 Neuroscience Available at: http://www.nature.com/neuro/journal/vaop/ncurrent/full/nn.4436.html.

954 Lee S, Kruglikov I, Huang ZJ, Fishell G, Rudy B (2013) A disinhibitory circuit mediates motor
955 integration in the somatosensory cortex. Nature Neuroscience 16:1662–1670 Available at:
956 https://www.nature.com/articles/nn.3544.

957 Licata AM, Kaufman MT, Raposo D, Ryan MB, Sheppard JP, Churchland AK (2017) Posterior Parietal
958 Cortex Guides Visual Decisions in Rats. J Neurosci 37:4954–4966.

959 Lin P-A, Asinof SK, Edwards NJ, Isaacson JS (2019) Arousal regulates frequency tuning in primary
960 auditory cortex. Proc National Acad Sci 116:25304–25310.

961 Livingstone MS, Hubel DH (1981) Effects of sleep and arousal on the processing of visual information in
962 the cat. Nature 291:554–561.

963 Madisen L, Zwingman TA, Sunkin SM, Oh SW, Zariwala HA, Gu H, Ng LL, Palmiter RD, Hawrylycz
964 MJ, Jones AR, Lein ES, Zeng H (2009) A robust and high-throughput Cre reporting and
965 characterization system for the whole mouse brain. Nature Neuroscience 13:133–140 Available at:
966 http://www.nature.com/neuro/journal/v13/n1/full/nn.2467.html.

967 Marrocco RT, Witte EA, Davidson MC (1994) Arousal systems. Curr Opin Neurobiol 4:166–170.

968 Mayo JP, Cohen MR, Maunsell JHR (2015) A Refined Neuronal Population Measure of Visual Attention.
969 Plos One 10:e0136570.

McGinley MJ, David SV, McCormick DA (2015) Cortical Membrane Potential Signature of Optimal States for Sensory Signal Detection. Neuron 87:179–192.

Minderer M, Brown KD, Harvey CD (2019) The Spatial Structure of Neural Encoding in Mouse Posterior Cortex during Navigation. Neuron.

Mineault PJ, Tring E, Trachtenberg JT, Ringach DL (2016) Enhanced Spatial Resolution During Locomotion and Heightened Attention in Mouse Primary Visual Cortex. The Journal of neuroscience : the official journal of the Society for Neuroscience 36:6382–6392 Available at: http://www.jneurosci.org/content/36/24/6382.short.

Morcos AS, Harvey CD (2016) History-dependent variability in population dynamics during evidence accumulation in cortex. Nat Neurosci 19:1672–1681.

Musall S, Kaufman MT, Juavinett AL, Gluf S, Churchland AK (2019) Single-trial neural dynamics are dominated by richly varied movements. Nat Neurosci 22:1677–1686.

Niell CM, Stryker MP (2010) Modulation of Visual Responses by Behavioral State in Mouse Visual Cortex. Neuron 65:472–479 Available at: https://www.sciencedirect.com/science/article/pii/S0896627310000590.

Nitz DA (2006) Tracking route progression in the posterior parietal cortex. Neuron 49:747–756 Available at: http://eutils.ncbi.nlm.nih.gov/entrez/eutils/elink.fcgi?dbfrom=pubmed&;id=16504949&retmode=ref&cmd=prlinks.

Pachitariu M, Stringer C, Dipoppa M, Schröder S, Rossi LF, Dalgleish H, Carandini M, Harris KD (2017) Suite2p: beyond 10,000 neurons with standard two-photon microscopy. Biorxiv:061507.

Pakan JM, Lowe SC, Dylda E, Keemink SW, Currie SP, Coutts CA, Rochefort NL (2016) Behavioral-state modulation of inhibition is context-dependent and cell type specific in mouse visual cortex. Elife 5:e14985.

Panzeri S, Moroni M, Safaai H, Harvey CD (2022) The structures and functions of correlations in neural population codes. Nat Rev Neurosci 23:551–567.

Park IM, Meister MLR, Huk AC, Pillow JW (2014) Encoding and decoding in parietal cortex during sensorimotor decision-making. Nature Neuroscience 17:1395–1403.

Pfeffer CK, Xue M, He M, Huang ZJ, Scanziani M (2013) Inhibition of Inhibition in Visual Cortex: The Logic of Connections Between Molecularly Distinct Interneurons. Nat Neurosci 16:1068–1076.

Pho GN, Goard MJ, Woodson J, Crawford B, Sur M (2018) Task-dependent representations of stimulus and choice in mouse parietal cortex. Nat Commun 9:2596.

Pi H-J, Hangya B, Kvitsiani D, Sanders JI, Huang ZJ, Kepecs A (2013) Cortical interneurons that specialize in disinhibitory control. Nature 503:521–524.

1004 Pillow JW, Shlens J, Paninski L, Sher A, Litke AM, Chichilnisky EJ, Simoncelli EP (2008) Spatio-
1005 temporal correlations and visual signalling in a complete neuronal population. Nature 454:995–999
1006 Available at: http://www.nature.com/doifinder/10.1038/nature07140.

1007 Pinto L, Goard MJ, Estandian D, Xu M, Kwan AC, Lee S-H, Harrison TC, Feng G, Dan Y (2013) Fast
1008 modulation of visual perception by basal forebrain cholinergic neurons. Nat Neurosci 16:1857–1863.

1009 Polack P-O, Friedman J, Golshani P (2013) Cellular mechanisms of brain state–dependent gain
1010 modulation in visual cortex. Nat Neurosci 16:1331–1339.

1011 Poulet JFA, Petersen CCH (2008) Internal brain state regulates membrane potential synchrony in barrel
1012 cortex of behaving mice. Nature 454:881–885.

1013 Rikhye RV, Yildirim M, Hu M, Breton-Provencher V, Sur M (2021) Reliable sensory processing in
1014 mouse visual cortex through cooperative interactions between somatostatin and parvalbumin
1015 interneurons. J Neurosci:JN-RM-3176-20.

1016 Runyan CA, Piasini E, Panzeri S, Harvey CD (2017) Distinct timescales of population coding across
1017 cortex. Nature 548:92–96 Available at:
1018 http://www.nature.com/nature/journal/v548/n7665/full/nature23020.html?foxtrotcallback=true.

1019 Saderi D, Schwartz ZP, Heller CR, Pennington JR, David SV (2021) Dissociation of task engagement and
1020 arousal effects in auditory cortex and midbrain. Elife 10:e60153.

1021 Schneider DM, Nelson A, Mooney R (2014) A synaptic and circuit basis for corollary discharge in the
1022 auditory cortex. Nature 513:189–194 Available at:
1023 http://www.nature.com/nature/journal/v513/n7517/full/nature13724.html.

1024 Shimaoka D, Harris KD, Carandini M (2018) Effects of Arousal on Mouse Sensory Cortex Depend on
1025 Modality. Cell Reports 25:3230.

1026 Stitt I, Zhou ZC, Radtke-Schuller S, Fröhlich F (2018) Arousal dependent modulation of thalamo-cortical
1027 functional interaction. Nat Commun 9:2455.

1028 Stringer C, Pachitariu M, Steinmetz N, Reddy CB, Carandini M, Harris KD (2019) Spontaneous
1029 behaviors drive multidimensional, brainwide activity. Science 364:eaav7893.

1030 Taniguchi H, He M, Wu P, Kim S, Paik R, Sugino K, Kvitsiani D, Kvitsani D, Fu Y, Lu J, Lin Y,
1031 Miyoshi G, Shima Y, Fishell G, Nelson SB, Huang ZJ (2011) A resource of Cre driver lines for
1032 genetic targeting of GABAergic neurons in cerebral cortex. Neuron 71:995–1013 Available at:
1033 http://dx.doi.org/10.1016/j.neuron.2011.07.026.

1034 Tremblay R, Lee S, Rudy B (2016) GABAergic Interneurons in the Neocortex: From Cellular Properties
1035 to Circuits. Neuron 91:260–292 Available at:
1036 http://www.sciencedirect.com/science/article/pii/S0896627316303117.

1037 Tseng S-Y, Chettih SN, Arlt C, Barroso-Luque R, Harvey CD (2022) Shared and specialized coding
1038 across posterior cortical areas for dynamic navigation decisions. Neuron 110:2484-2502.e16.

Valente M, Pica G, Bondanelli G, Moroni M, Runyan CA, Morcos AS, Harvey CD, Panzeri S (2021) Correlations enhance the behavioral readout of neural population activity in association cortex. Nat Neurosci 24:975–986.

Veit J, Hakim R, Jadi MP, Sejnowski TJ, Adesnik H (2017) Cortical gamma band synchronization through somatostatin interneurons. Nature Neuroscience 20:951–959.

Vinck M, Batista-Brito R, Knoblich U, Cardin JA (2015) Arousal and Locomotion Make Distinct Contributions to Cortical Activity Patterns and Visual Encoding. Neuron 86:740–754.

Wang X-J, Yang GR (2018) A disinhibitory circuit motif and flexible information routing in the brain. Curr Opin Neurobiol 49:75–83.

Waschke L, Tune S, Obleser J (2019) Local cortical desynchronization and pupil-linked arousal differentially shape brain states for optimal sensory performance. Elife 8:e51501.

Whitlock JR, Pfuhl G, Dagslott N, Moser M-B, Moser EI (2012) Functional split between parietal and entorhinal cortices in the rat. Neuron 73:789–802 Available at: http://eutils.ncbi.nlm.nih.gov/entrez/eutils/elink.fcgi?dbfrom=pubmed&;id=22365551&retmode=ref&cmd=prlinks.

Wilson NR, Runyan CA, Wang FL, Sur M (2012) Division and subtraction by distinct cortical inhibitory networks in vivo. Nature 488:343–348 Available at: http://eutils.ncbi.nlm.nih.gov/entrez/eutils/elink.fcgi?dbfrom=pubmed&;id=22878717&retmode=ref&cmd=prlinks.

Xiang Z, Huguenard JR, Prince DA (1998) Cholinergic switching within neocortical inhibitory networks. Science 281:985–988 Available at: http://www.sciencemag.org/cgi/content/full/281/5379/985.

Xu H, Jeong H-Y, Tremblay R, Rudy B (2013) Neocortical Somatostatin-Expressing GABAergic Interneurons Disinhibit the Thalamorecipient Layer 4. Neuron 77:155–167 Available at: http://www.sciencedirect.com/science/article/pii/S0896627312009956#.

Yavorska I, Wehr M (2021) Effects of Locomotion in Auditory Cortex Are Not Mediated by the VIP Network. Front Neural Circuit 15:618881.

Zhou M, Liang F, Xiong XR, Li L, Li H, Xiao Z, Tao HW, Zhang LI (2014) Scaling down of balanced excitation and inhibition by active behavioral states in auditory cortex. Nature Neuroscience 17:841–850.

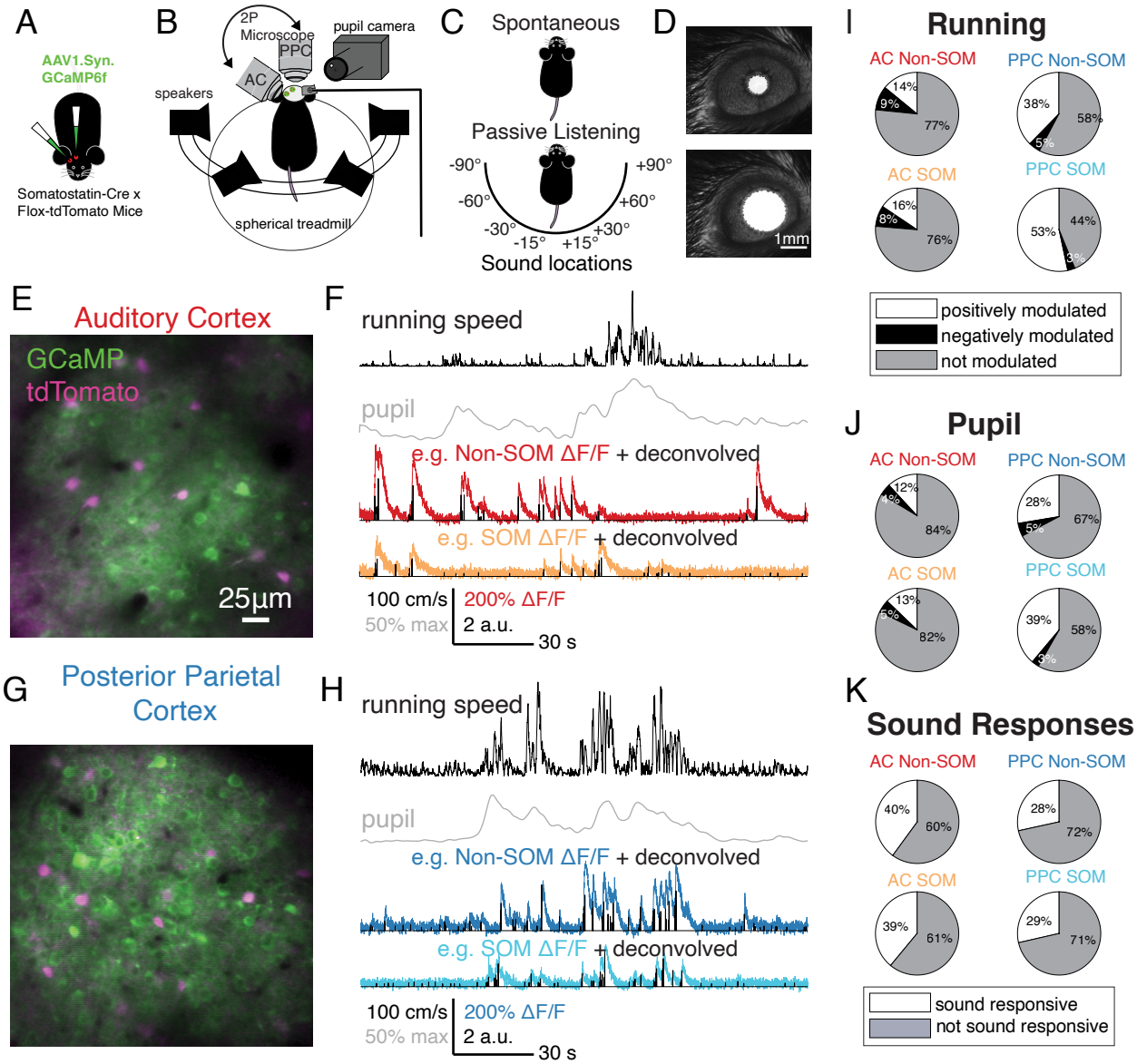

Figure 1: Imaging spike-related activity in SOM and Non-SOM neurons during behavioral state transitions. (A) Viral injections and cranial windows were made over auditory cortex (AC) and posterior parietal cortex (PPC) in each SOM-tdTomato mouse. (B) In imaging sessions, mice were headfixed over a spherical treadmill and allowed to run voluntarily. Four speakers arranged around the head presented sound stimuli. An infrared camera was used to image the pupil, and a rotating two-photon microscope was focused on either AC or PPC on a given imaging day. (C) Each imaging session included "Spontaneous" and "Passive Listening" contexts, without or with randomly presented sound stimuli from each of eight locations, respectively. (D) Pupil area was monitored via the pupil camera, scalebar in bottom image applies to top (constricted pupil) and bottom (dilated pupil). (E) Example field of view from auditory cortex, with intermingled tdTomato+/SOM+ (magenta) and tdTomato-/SOM- neurons, co-expressing GCaMP6f (green). (F) Example aligned behavioral and neural signals collected during the imaging session in E, including running speed (cm/s), normalized pupil area, dF/F from a Non-SOM (red) and SOM neuron (orange), each overlaid with the neuron's deconvolved estimated spike rates. (G) As in E, for an example posterior parietal cortex field of view. (H) As in F, for the PPC field of view in G. (I) Proportions of Non-SOM and SOM neurons in AC (left) and PPC (right) with significant positive (white), negative (black), or no modulation by mouse's running onset (gray). AC Non-SOM N=2645; AC SOM N=359; PPC Non-SOM N=4719; PPC SOM N=525. (J) As in I, for pupil dilation. (K) Proportion of Non-SOM and SOM neurons in AC and PPC that were significantly sound responsive to at least one location (white) or not significantly sound responsive (gray).

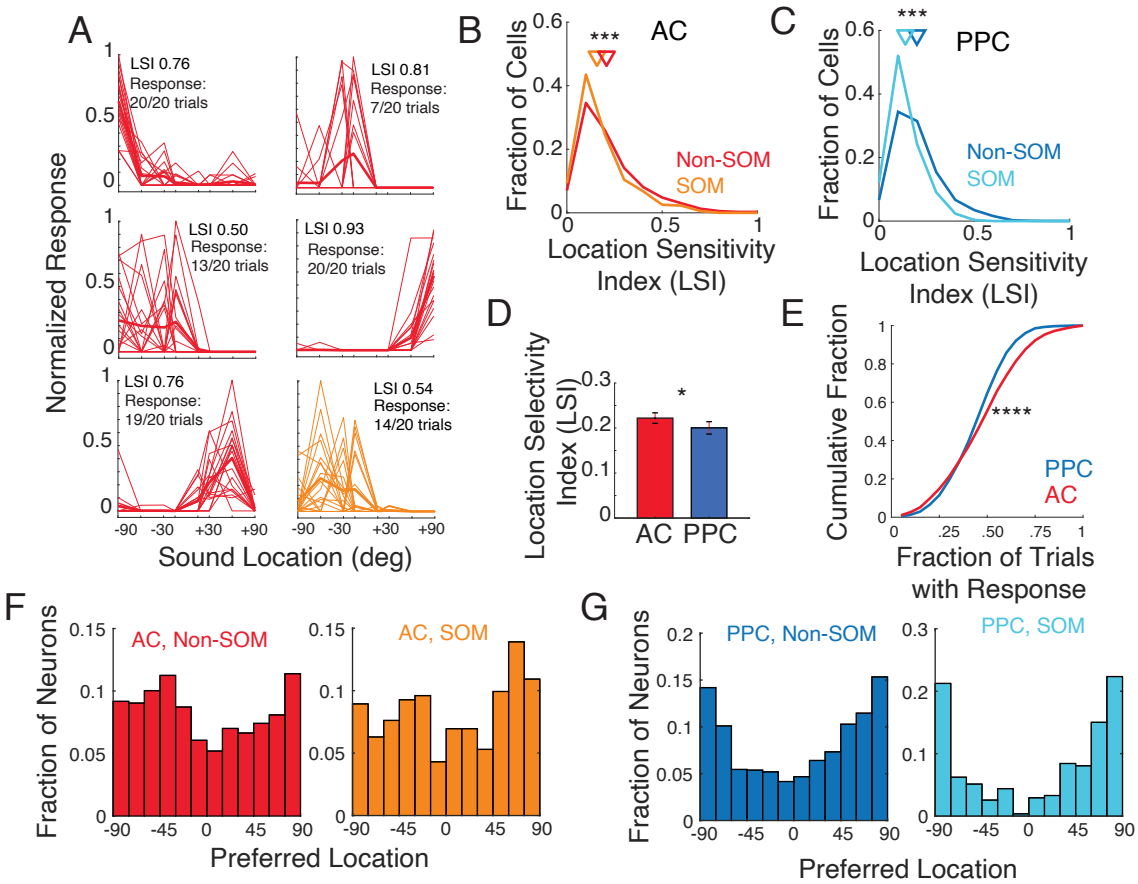

Figure 2: Sound Location Sensitivity in AC and PPC. (A) Six example neurons with diverse sound location preferences, ranging from ipsilateral (-90 - 0 degrees) to contralateral locations (0 - +90 degrees). Thin lines: mean response during sound presentation of individual trials. Thick lines: Trial average. The location sensitivity index (LSI) and response reliability are reported for each example cell. Red: Example Non-SOM neurons. Orange: Example SOM neuron. (B) Distribution of Location Sensitivity Index (LSI) for Non-SOM (0.20 [0.20, 0.21] , N=2455) and SOM (.19 [0.18, .19], N=354) neurons in AC. Triangles indicate population means. (C) As in B, for PPC Non-SOM (0.20 [0.19, 0.20], N=2553) and SOM (.13 [.12, .14], N=298). (D) Mean location selectivity index in AC and PPC. (E) Cumulative distributions of response reliability, the fraction of sound-responsive trials, in AC and PPC. (F) Histograms of the preferred locations of all AC Non-SOM and SOM neurons with LSI's>0.05. (G) Histograms of the preferred locations of all PPC Non-SOM and SOM neurons with LSI's>0.05. * p<0.05, ***p<0.001, ****p<0.0001, error bars indicate SEM.

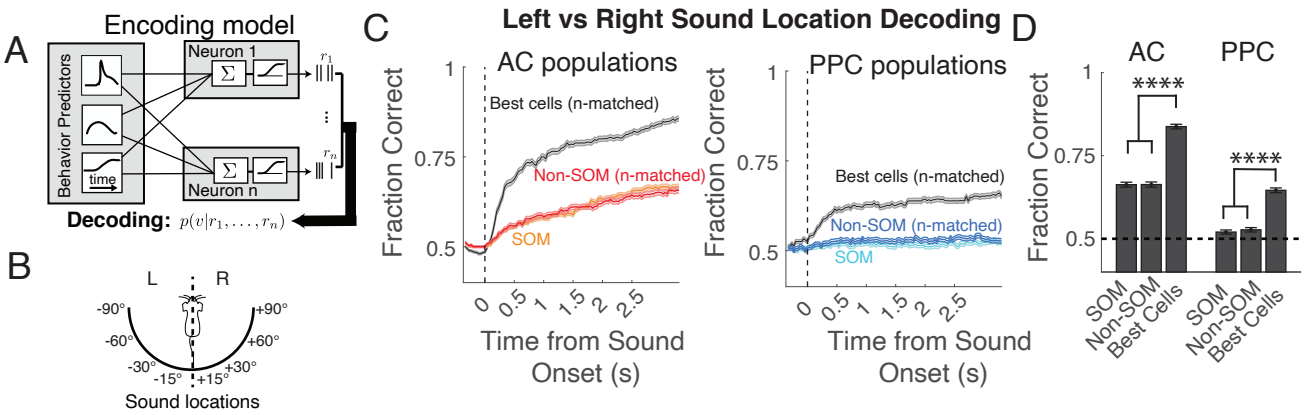

Figure 3: Decoding Sound Location from AC and PPC Population Activity. (A) The encoding model was trained on all trials that included all arousal levels, and inverted using Bayes Rule to compute the posterior probability of auditory stimuli given the activity of the neural population in AC and PPC . (B) Schematic of the discrimination being performed by the decoder, classifying sound stimuli as occuring from the left or right of the mouse. (C) Left: Mean cumulative population decoder performance (across datasets) when classifying left vs right locations, when based on “best cells”, defined as individual Non-SOM cells or SOM cells with the highest decoding performance. “Best cells” and Non-SOM cells in each dataset were subsampled to match the N of the SOM neuron population within each imaging field of view. Right: Population decoder performance using PPC neurons. Chance performance is 0.5. (D) Mean decoder performance using all timepoints in the trial (equivalent to the final timepoints in (C) using SOM neurons, subsampled Non-SOM neurons, and “best cells” in AC and PPC. Dotted line corresponds to chance performance (50%). N=24 AC datasets, N=20 PPC datasets. Error bars indicate SEM. ****p<0.0001.

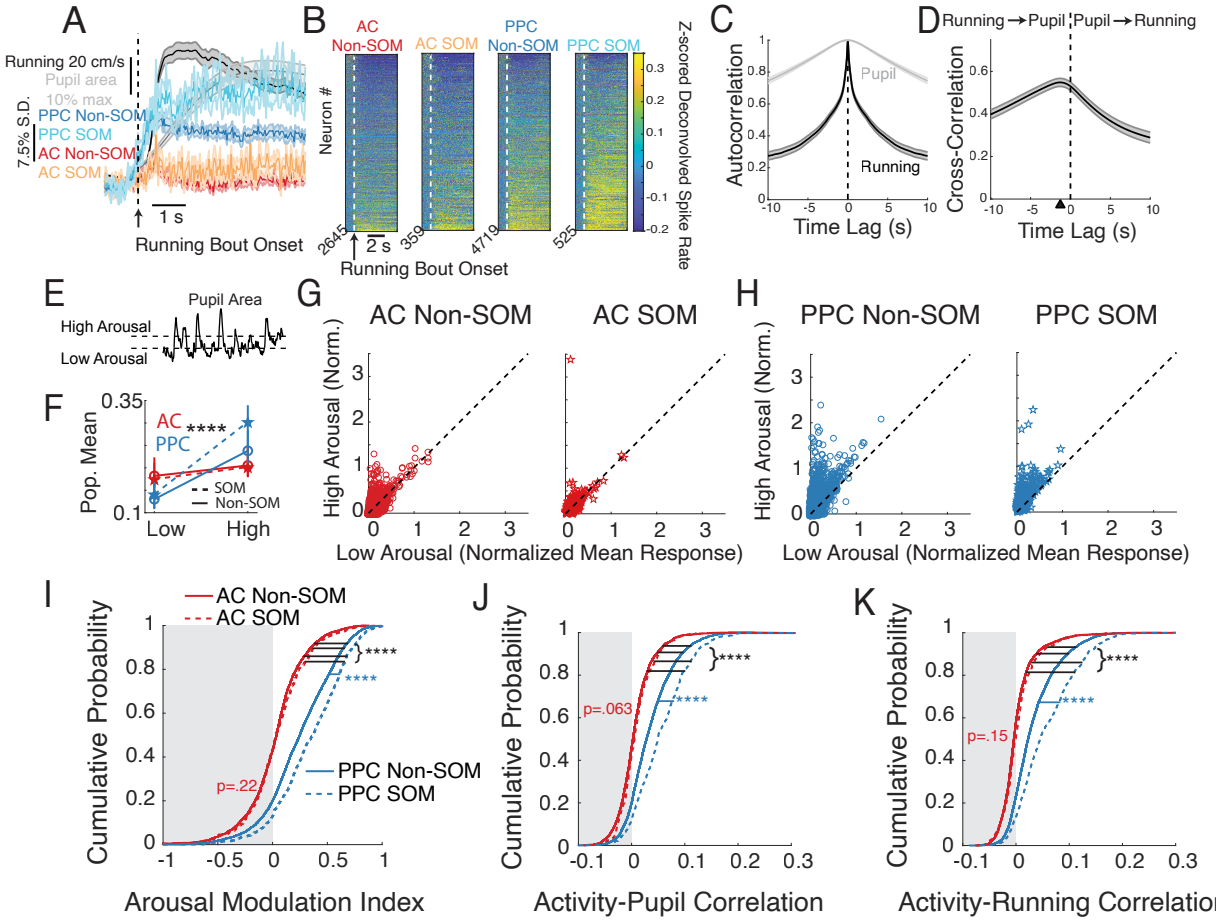

Figure 4: Single cell activity changes with arousal during the spontaneous context. (A) Average z-scored deconvolved activity, running speed, and pupil area aligned on running bout onset. Red: AC Non-SOM neurons' activity (N=24 datasets), Orange: AC SOM neurons' activity (N=24 datasets), Dark Blue: PPC Non-SOM neurons' activity (N=20 datasets), Light Blue: PPC SOM neurons' activity (N=20 datasets), Black: Running speed (N=44 datasets), Gray: Pupil area (N=44 datasets). (B) Average z-scored deconvolved activity of individual neurons, from L to R: all AC Non-SOM, AC SOM, PPC Non-SOM, and PPC SOM neurons aligned on running bout onset (AC Non-SOM N=2645; AC SOM N=359; PPC Non-SOM N=4719; PPC SOM N=525, in B-I). Neurons were sorted by running modulation. (C) Autocorrelation of pupil area and running speed, averaged across all datasets (N=44). (D) Cross-correlation between running speed and pupil area, averaged across all datasets (N=44). Black triangle indicates time lag with peak correlation, with running preceding pupil by 1.27 s. (E) Illustration of clustering that sorted pupil area during each imaging frame into low, transition, and high arousal states. (F) Mean responses of AC Non-SOM (red solid), AC SOM (red dotted), PPC Non-SOM (blue solid), and PPC SOM (blue dotted) neurons in low and high arousal states, as defined in E. (G) Left: Mean activity of AC Non-SOM neurons in high arousal state (classified with clustering as in E), plotted against mean activity in the low arousal state. Right: Mean activity of AC SOM neurons in high arousal vs low arousal states. (H) As in G, for PPC Non-SOM and SOM neurons. (I) Cumulative probability distribution of the arousal modulation index in AC Non-SOM (solid red), AC SOM (dotted red), PPC Non-SOM (solid blue), and PPC SOM (dotted blue) neurons. Arousal modulation index was calculated from the values in G-H, (High-Low)/(High+Low) for each neuron. (J) Cumulative probability distribution of the Pearson correlation between each neuron's activity and pupil area, colors as in I. (K) Cumulative probability distribution of the Pearson correlation between each neuron's activity and running speed. Significance as indicated, permutation test, **** p<.0001. Error bars: 95% bootstrapped confidence interval around the mean.

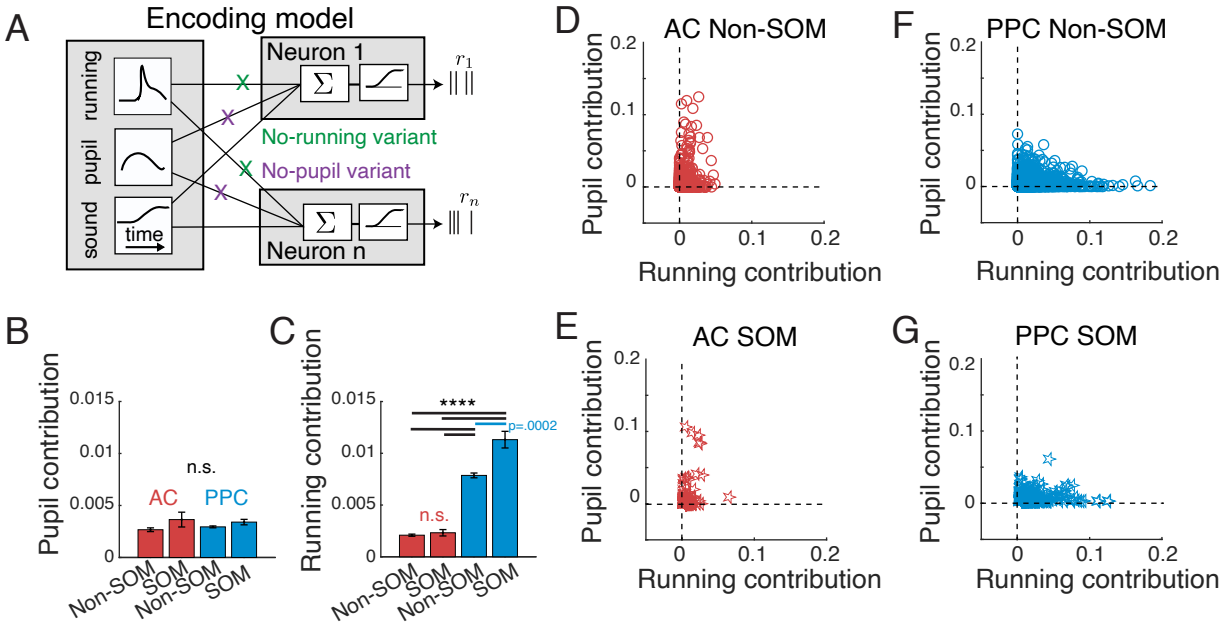

Figure 5: Using an Encoding Model to Disentange Running and Pupil Contributions to Single Cell Activity. (A) Schematic of Generalized Linear Model (GLM) used to determine the unique contributions of pupil area and running velocity to neurons' activity. (B) Average contribution of pupil area to activity across all AC Non-SOM (N=2645) and SOM (N=359) neurons (red bars) and PPC Non-SOM (N=4525) and SOM (N=505) neurons (blue bars). Contribution was quantified as the improvement in model prediction performance of each neuron's activity when adding pupil area as a set of predictors. Errorbars indicate SEM, n.s., not significant, exact values in text. (C) As in B, calculated when comparing model performance with and without running velocity predictors. AC Non-SOM and SOM neurons (red bars) and PPC Non-SOM and SOM neurons (blue bars), ****p<.0001. (D) Pupil contribution plotted against running contribution for each AC Non-SOM neuron, calculated as in B. (E) Pupil contribution plotted against running contribution for each AC SOM neuron. (F-G) Pupil contribution plotted against running contribution for each PPC Non-SOM or SOM neuron. Sample sizes in B apply to all panels.

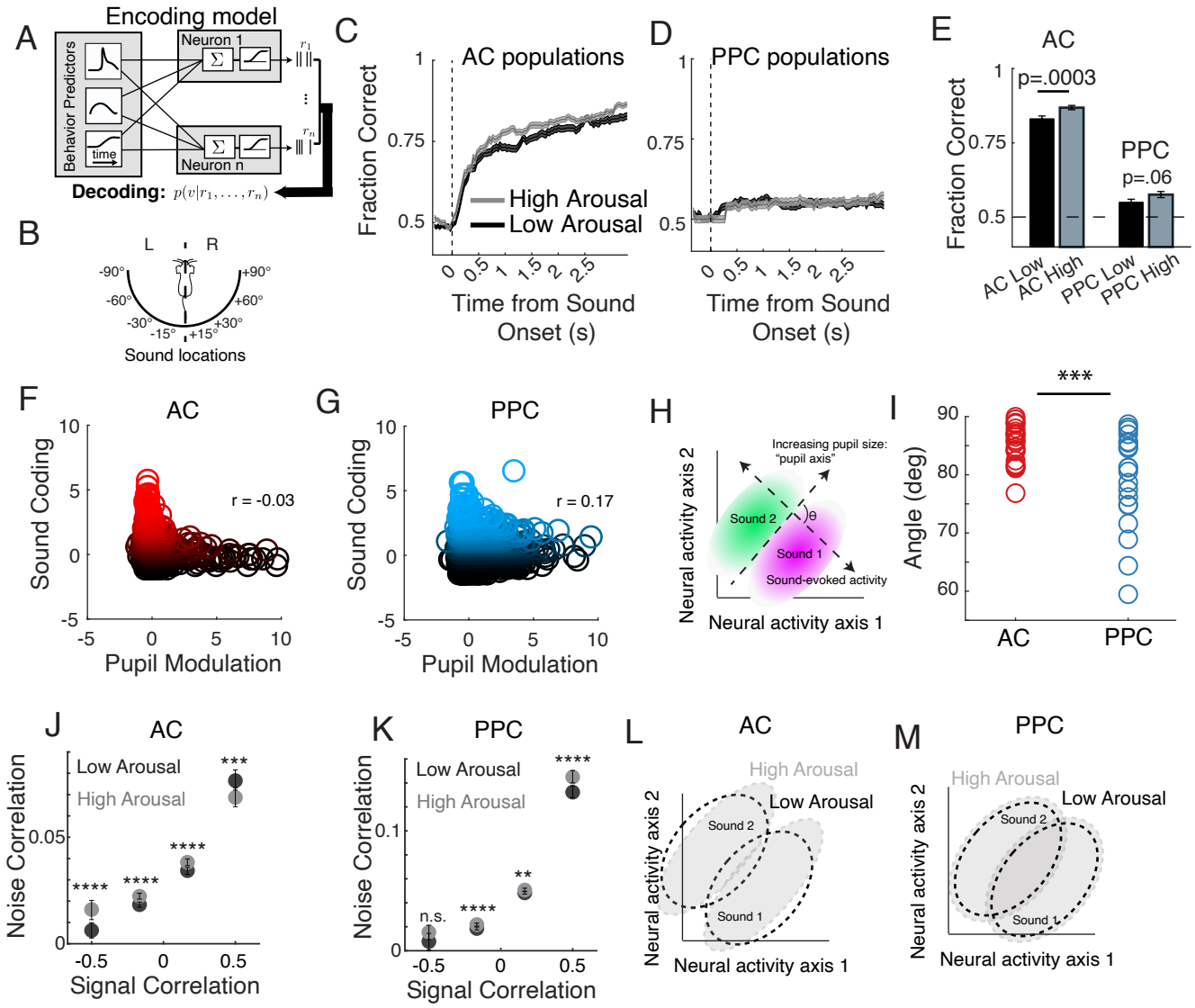

Figure 6: Arousal impacts the structure of population activity, improving information coding in AC. (A) The encoding model was trained on all trials that included all arousal levels, and inverted using Bayes Rule to compute the posterior probability of auditory stimuli given the activity of the neural population in AC and PPC. (B) Schematic of the discrimination being performed by the decoder, classifying sound stimuli as occuring from the left or right of the mouse. (C) Mean fraction correct of cumulative sound location (left sound locations vs right sound locations) decoding in AC (right) and PPC (left) populations in high (dark) and low (light) arousal conditions. Subsampling to match arousal and sound locations was repeated 10x. (D) Cumulative fraction correct of decoding for left vs right sound location at the end of the trial in AC and PPC. (F) For each AC neuron, the sound location decoding performance based on that neuron's activity is plotted against that neuron's pupil modulation, as quantified by the encoding model in Figure 5. Neurons are color-coded from black to red to indicate their z-scored sound location decoding performance (red neurons > 0 z-scored performance). (G) As in F, for PPC. (H) Schematic to explain the definitions of the sound location and pupil axes in high dimensional population activity space in I. (I) Angle in degrees between the pupil and sound location axes in each AC and PPC dataset. The angle between the pupil and sound axes is significantly smaller in PPC than AC. (J) Mean pairwise noise correlation among sound responsive AC neurons during high arousal (gray) and low arousal (black) trials, binned by their pairwise signal correlation. (K) As in (J), but for PPC. (L) Schematic demonstrating the impacts of arousal on sound coding in AC population activity. The shape of the population activity subspace responding to "sound 1" and "sound 2" changes between low arousal (dashed outlines) and high arousal (gray ovals) states, improving their discriminability. This shape change occurs because the shared variability is reduced among neurons coding for similar locations, and enhanced among neurons coding for different locations (see J). (M) As in L, for PPC. In PPC, the shape of the area of population activity space encoding sound 1 or sound 2 does not change with arousal, as shared variability is more generally increased across neuron pairs (see K). Across panels, ** p<0.01, *** p<0.001, **** p<0.0001, n.s. not significant. AC Non-SOM N=24 datasets; AC SOM N=24 datasets; PPC Non-SOM N=20 datasets; PPC SOM N=20 datasets throughout figure panels.

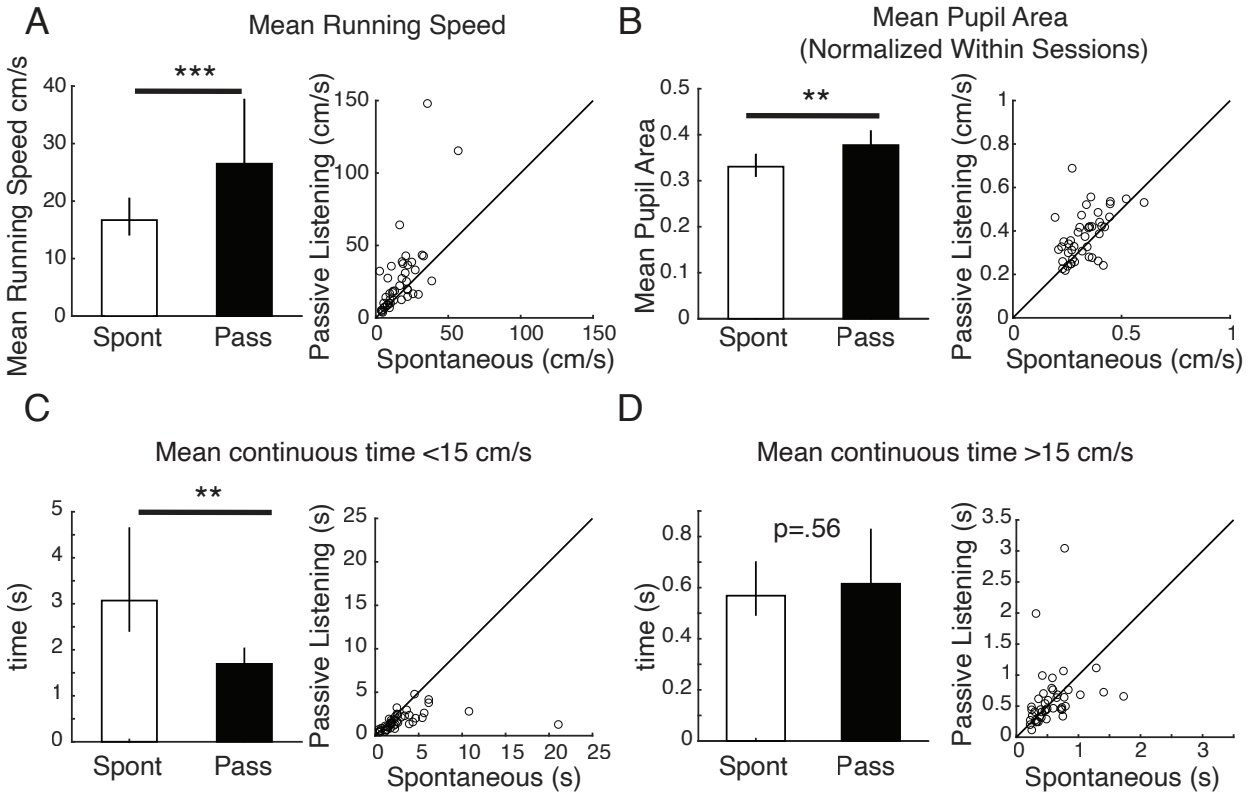

Figure S1: Characterizing running behavior and pupil size across contexts. (A) Left: Mean running speed in the spontaneous and passive listening behavioral contexts. Right: Mean running speed during the passive listening context plotted against the mean running speed during the spontaneous context, for each imaging session, p=.0003. (B) Left: Mean, maximum normalized pupil area during the spontaneous and passive listening contexts. Right: Mean pupil area in the two contexts for each imaging session. p=.002. (C) Left: Mean time spent running less than 15 cm/s in spontaneous and passive listening contexts. Right: Time spent running less than 15 cm/s during the two contexts, for each imaging session, p<.0001. (D) Left: Mean time spent running faster than15 cm/s in spontaneous and passive listening contexts. Right: Time spent running faster than 15 cm/s in the two contexts, for each imaging session. N=44 imaging sessions for all panels. Error bars indicate bootstrapped 95% confidence intervals, ***p<0.001; **p<.01.

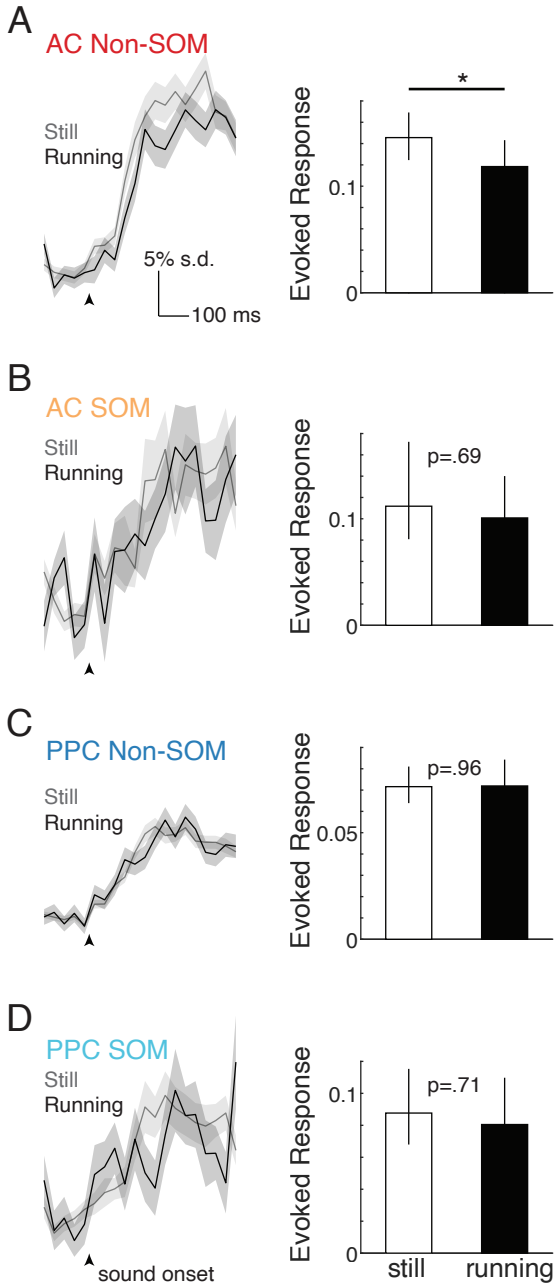

Figure S2: Sound evoked responses during periods of stillness and running (A) Left: Sound-evoked activity of sound-responsive AC Non-SOM neurons (See: Figure 1K, Materials and Methods), in response to the preferred sound location. Gray: Responses during trials when mice were running less than 15 cm/s. Black: Responses during trials when mice were running faster than 20 cm/s. Sound-evoked activity was baseline-subtracted using the preceding 240 ms window for ease of display. Black arrow indicates sound onset. Right: Mean sound-evoked activity during the first 500ms of sound presentation during still and running periods, n=432, p=0.017 (paired permutation test with 10,000 iterations here, and throughout). Subsampling to match locomotion condition and repetition was repeated 10x for each sound location. (B) As in A, for AC SOM neurons, n=59 (C) As in A-B for PPC Non-SOM neurons, n=901 (D) As in A-C for PPC SOM neurons, n=112, *p<0.05.

Table 1: Sound Location Decoding

Group	n	Mean	Standard Deviation	95% Confidence Interval of the Mean	p value
AC Best Cells – LR[1]	24 x 10	0.86	0.11	0.85-0.87	
AC Non-SOM – LR[2]	24 x 10	0.68	0.13	0.66-0.69	
AC SOM – LR[3]	24 x 10	0.68	0.12	0.66-0.69	
PPC Best Cells – LR[4]	20 x 10	0.65	0.10	0.64-0.67	
PPC Non-SOM – LR[5]	20 x 10	0.53	0.09	0.52-0.53	
PPC SOM – LR[6]	20 x 10	0.52	0.09	0.51-0.53	
Kruskal Wallis[1-6]					<0.0001
Unpaired permutation[1,2]					<0.0001
Unpaired permutation[1,3]					<0.0001
Unpaired permutation[1,4]					<0.0001
Unpaired permutation[1,5]					<0.0001
Unpaired permutation[1,6]					<0.0001
Unpaired permutation[2,3]					0.8167
Unpaired permutation[2,4]					0.1189
Unpaired permutation[2,5]					<0.0001
Unpaired permutation[2,6]					<0.0001
Unpaired permutation[3,4]					0.1160
Unpaired permutation[3,5]					<0.0001
Unpaired permutation[3,6]					<0.0001
Unpaired permutation[4,5]					<0.0001
Unpaired permutation[4,6]					<0.0001
Unpaired permutation[5,6]					0.4644
AC High Arousal – LR (All cells)	24 x 10	0.83	0.16	0.81-0.85	0.0003
AC Low Arousal – LR (All cells)	24 x 10	0.78	0.12	0.76-0.80	
PPC High Arousal – LR (All cells)	20 x 10	0.54	0.13	0.53-0.55	0.060
PPC Low Arousal – LR (All cells)	20 x 10	0.57	0.13	0.56-0.59	

Table 2: Arousal Modulation Index during spontaneous context

Group	n	Mean	Standard Deviation	95% Confidence Interval of the Mean	p value
AC SOM arousal modulation index[1]	359	0.057	0.29	0.027-0.085	
AC Non-SOM, arousal modulation index[2]	2645	0.035	0.28	0.025-0.046	
PPC Non-SOM arousal modulation index[3]	4719	0.25	0.31	0.24-0.26	
PPC SOM arousal modulation index[4]	525	0.35	0.31	0.32-0.37	
Kruskal Wallis[1-4]					7.2E-12
Unpaired permutation[1,2]					0.22
Unpaired permutation,[1,3]					<0.0001
Unpaired permutation,[2,3]					<0.0001
Unpaired permutation,[1,4]					<0.0001
Unpaired permutation,[2,4]					<0.0001
Unpaired permutation,[3,4]					<0.0001

Table 3: Correlation coefficients with pupil area and running speed during spontaneous context

Group	n	Mean	Standard Deviation	95% Confidence Interval of the Mean	p value
AC Non-SOM, pupil correlation coefficient[1]	2645	0.0057	0.033	0.0045-0.0070	
AC SOM pupil correlation coefficient[2]	359	0.0091	0.031	0.0061-0.12	
PPC Non-SOM pupil correlation coefficient[3]	4719	0.035	0.043	0.034-0.036	
PPC SOM pupil correlation coefficient[4]	525	0.055	0.049	0.051-0.059	
Kruskal Wallis[1-4]					6.3E-250
Unpaired permutation[1,2]					0.063
Unpaired permutation[,1,3]					<0.0001
Unpaired permutation[,2,3]					<0.0001
Unpaired permutation[,1,4]					<0.0001
Unpaired permutation[,2,4]					<0.0001
Unpaired permutation[,3,4]					<0.0001
AC Non-SOM, running speed correlation coefficient[1]	2645	0.0020	0.034	0.00060-0.0033	
AC SOM running speed correlation coefficient[2]	359	0.0048	0.034	0.0013-0.0089	
PPC Non-SOM running speed correlation coefficient[3]	4719	0.033	0.044	0.032-0.034	
PPC SOM running speed correlation coefficient[4]	525	0.057	0.055	0.053-0.062	
Kruskal Wallis[1-4]					<0.0001
Unpaired permutation[1,2]					0.15
Unpaired permutation[,1,3]					<0.0001
Unpaired permutation[,2,3]					<0.0001
Unpaired permutation[,1,4]					<0.0001
Unpaired permutation[,2,4]					<0.0001
Unpaired permutation[,3,4]					<0.0001

Table 4: Arousal Modulation Index during passive listening context

Group	n	Mean	Standard Deviation	95% Confidence Interval of the Mean	p value
AC Non-SOM, arousal modulation index[1]	2645	0.072	0.26	0.063-0.083	
AC SOM arousal modulation index[2]	359	0.079	0.28	0.049-0.11	
PPC Non-SOM arousal modulation index[3]	4719	0.18	0.29	0.17-0.19	
PPC SOM arousal modulation index[4]	525	0.26	0.28	0.24-0.29	
Kruskal Wallis[1-4]					2.1E-66
Unpaired permutation[1,2]					0.63
Unpaired permutation,[1,3]					<0.0001
Unpaired permutation,[2,3]					<0.0001
Unpaired permutation,[1,4]					<0.0001
Unpaired permutation,[2,4]					<0.0001
Unpaired permutation,[3,4]					<0.0001

Table 5: Correlation coefficients with pupil area and running speed during passive listening context

Group	n	Mean	Standard Deviation	95% Confidence Interval of the Mean	p value
AC Non-SOM, pupil correlation coefficient[1]	2645	0.0096	0.031	0.0081-0.010	
AC SOM pupil correlation coefficient[2]	359	0.010	0.033	0.0074-0.014	
PPC Non-SOM pupil correlation coefficient[3]	4719	0.030	0.042	0.029-0.031	
PPC SOM pupil correlation coefficient[4]	525	0.043	0.044	0.038-0.046	
Kruskal Wallis[1-4]					5.3E-115
Unpaired permutation[1,2]					0.63
Unpaired permutation,[1,3]					<0.0001
Unpaired permutation,[2,3]					<0.0001
Unpaired permutation,[1,4]					<0.0001
Unpaired permutation,[2,4]					<0.0001
Unpaired permutation,[3,4]					<0.0001
AC Non-SOM, running speed correlation coefficient[1]	2645	0.0067	0.029	0.0056-0.0078	
AC SOM running speed correlation coefficient[2]	359	0.0076	0.30	0.0050-0.011	
PPC Non-SOM running speed correlation coefficient[3]	4719	0.029	0.042	0.028-0.030	
PPC SOM running speed correlation coefficient[4]	525	0.045	0.047	0.038-0.046	
Kruskal Wallis[1-4]					1.2E-146
Unpaired permutation[1,2]					0.59
Unpaired permutation,[1,3]					<0.0001
Unpaired permutation,[2,3]					<0.0001
Unpaired permutation,[1,4]					<0.0001
Unpaired permutation,[2,4]					<0.0001
Unpaired permutation,[3,4]					<0.0001

Table 6: Pupil and Running Contributions

Group	n	Mean	Standard Deviation	95% Confidence Interval of the Mean	p value
AC Non-SOM, pupil diameter contribution[1]	2476	0.0027	0.0086	0.0023-0.0031	
AC SOM, pupil diameter contribution[2]	330	0.0036	0.0123	0.0025-0.0049	
PPC Non-SOM, pupil diameter contribution[3]	4525	0.0029	0.0060	0.0028-0.0031	
PPC SOM, pupil diameter contribution[4]	505	0.0034	0.0059	0.0029-.0040	
Kruskal Wallis[1-4]					<0.0001
Unpaired permutation[1,2]					0.0780
Unpaired permutation[,1,3]					0.1259
Unpaired permutation[,2,3]					0.2360
Unpaired permutation[,1,4]					0.0619
Unpaired permutation[,2,4]					0.9520
Unpaired permutation[,3,4]					0.1070
AC Non-SOM, running speed contribution[1]	2476	0.0020	0.0050	0.0019-0.0023	
AC SOM running speed contribution [2]	330	0.0023	0.0005	0.0019-0.0320	
PPC Non-SOM running speed contribution [3]	4525	0.0079	0.0156	0.0075-0.0083	
PPC SOM running speed contribution [4]	505	0.0113	0.0181	0.0099-0.0131	
Kruskal Wallis[1-4]					<0.0001
Unpaired permutation[1,2]					0.4409
Unpaired permutation[,1,3]					0.0001
Unpaired permutation[,2,3]					0.0001
Unpaired permutation[,1,4]					0.0001
Unpaired permutation[,2,4]					0.0001
Unpaired permutation[,3,4]					0.0002